Chapter 1

Feasibility of seismic monitoring

1.1 Overview

In this chapter, I present a methodology for performing a feasibility analysis to predict the likelihood of seismically detecting and monitoring changes in subsurface rock properties due to fluid flow. Given a geologic description of the subsurface, fluid-flow simulations are performed to predict the spatial distribution of flow pressure, temperature and fluid saturations. These fluid-flow parameters are mapped with rock physics transformations to seismic velocity and density models of the subsurface as a function of the flow simulation and geologic description. After upscaling to seismic wavelengths, seismic reflection data are then simulated and analyzed with realistic noise levels, acquisition parameters and survey errors, to determine if the predicted fluid flow can be detected and monitored with realistic seismic time-lapse data. A detailed feasibility analysis is presented for a case study in the Troll Field, offshore Norway, in which the goal is to determine whether gas coning at a horizontal oil depletion well can be monitored from time-lapse marine surface seismic data. [1]

1.2 Introduction

Hydrocarbon reservoirs are increasingly recognized as spatially heterogeneous entities in terms of lithology, porosity, permeability, and pore-fluid content. Knowledge of the spatial variation of these reservoir parameters is critical to accurately evaluate the total volume of recoverable hydrocarbon reserves in place, to predict fluid flow in the reservoir and associated physical processes such as heat or pressure transfer, and to project and monitor reservoir fluid recovery as a function of time.

Seismic time-lapse monitor surveys may help clarify the distribution and movement of fluids in a hydrocarbon reservoir during the process of oil and gas production,

[1] A modified version of this chapter was presented by Lumley et al. (?) at the Annual International SEG Conference, Los Angeles, CA, and received an Outstanding Paper Award.

e.g., Nur (?). However, repeated seismic surveys are expensive, and often it is not trivial to decide whether subtle fluid changes in deep reservoir rocks will be visible in surface seismic data, or what the optimal time interval for repeating seismic surveys should be. A responsible estimate of the magnitude and spatial coherency of seismic changes due to fluid flow with all available prior data under realistic conditions should be performed before survey design and data acquisition. This estimate can be defined as a *feasibility analysis* for time-lapse seismic monitoring.

1.2.1 Previous work

Although the concept of time-lapse seismic reservoir monitoring is relatively new, a few notable pilot projects have been conducted. Most early projects were attempted based on rock physics lab measurements which showed that large decreases in seismic velocity could be obtained in steam-heated cores of unconsolidated rock, Ito et al. (?), Wang and Nur (?). Pullin et al. (?) collected two pioneering 3-D seismic surveys before and after a steam pilot at an Athabasca tar sands reservoir site on this basis. Eastwood et al. (?) recently designed a similar 3-D seismic monitor experiment of an Alberta cyclic steam stimulation (CSS) project. Greaves and Fulp (?) won Best Paper for their design and analysis of a 3-D seismic monitoring experiment of an in situ combustion (fireflood) enhanced oil recovery (EOR) process.

While steam and fireflood seismic monitor experiments have confirmed large seismic velocity changes first predicted by lab measurements, the field response to more subtle fluid changes caused by primary oil depletion or waterflood is not well documented. Johnstad et al. (?) give one of the few of such case studies. They reported mixed results in their 4-D experiment over the Oseberg field while attempting to monitor the gascap movement under primary depletion in a difficult petrophysical and S/N environment.

However, an interesting situation is developing. Most producing fields world-wide have been covered by a 3-D seismic survey at some time in the 1980's or early 1990's. For a variety of good reasons, the time is ripe to re-survey many of these reservoirs with new 3-D seismic technology. This provides an opportunity to compare two 3-D data sets to see what has changed in the reservoir, and to calibrate the seismic changes with reservoir data. Feasibility analysis will be required to prioritize those reservoirs which have the best promise of showing meaningful seismic changes after years of production. This analysis should include reasonable flow simulation and history match data, core measurements and petrophysical data, seismic modeling of 3-D and offset-dependent effects, and seismic survey design and processing issues addressing modern versus vintage data problems such as positioning errors, shot and receiver geometry, variable S/N, and statistical versus deterministic data processing.

1.2.2 Optimal conditions for seismic monitoring

Some useful qualitative statements can be made about the feasibility of seismically monitoring fluid-flow changes. Ideal petrophysical conditions for observing seismic fluid flow changes require that the rock matrix has a low value of dry bulk modulus K_{dry}, as discussed in Chapter 2. This usually implies unconsolidated shallow sands and shales with high porosity and permeability, and uncemented grain contacts. In this case, if the oil in pore space has a low solution gas-oil ratio (GOR), a gas/fluid contact may be seismically visible, but it may be impossible to discern if the fluid is oil or water. Low GOR oils are unlikely to exhibit a seismic oil/water contact. On the other hand, if the oil has a high GOR value, then an oil/water contact may well be visible. The detection of a gas/oil or gas/water contact for high GOR oils depends upon the relative values of the bulk moduli for oil, water and gas. Any visible fluid contacts present in seismic data can be mapped from survey to survey in time-lapse mode, if the fluids are given enough time to move at least half a seismic wavelength.

In unconsolidated sediments, pore pressure variations may be observed by their effect on K_{dry}, and by changes in gas/oil saturation with respect to the bubble point pressure for a given oil. Temperature changes can be observed if viscous oils become more compressible when heated, or if pore fluids change to gas phase. Carbonate rocks are less likely to exhibit seismic changes during fluid flow since they tend to have low porosities and rigid dry rock moduli. However, fractured carbonates may behave like clastics and show velocity changes due to pore pressure and gas/fluid content. Also, secondary porosity caused by dissolution of carbonate rocks by carbonic acid in CO2, for example, may decrease the K_{dry} value enough to cause a visible seismic response.

Aside from petrophysical factors, seismic survey design, signal/noise issues, and seismic processing choices may hamper the ability to monitor fluid flow with time-lapse seismic data. Seismic experimental non-repeatability and survey positioning errors may mask any weak seismic anomaly that may have been originally present, as was probably a factor with the Oseberg case study (**?**). Multiple surveys acquired with variable fold, offset and azimuth coverage may lead to processing artifacts that dominate subtle seismic difference anomalies. Statistical data-dependent processing algorithms (e.g., deconvolution, amplitude balancing) may give inferior time-lapse results compared to model-based surface-consistent amplitude-preserved algorithms. The non-trivial nature of the seismic response to fluid-flow, petrophysics, and seismic data acquisition and processing, merits performing a careful feasibility analysis using all prior available site information before designing and acquiring seismic time-lapse data.

1.2.3 Current research

This chapter attempts to make a major step forward in establishing the petrophysical basis for seismic reservoir monitoring, by conducting a comprehensive physical modeling study that integrates fluid-flow simulation and rock physics with seismic modeling and imaging. I demonstrate the feasibility of performing seismic reservoir

monitoring with a case study in the Troll Field in the North Sea, offshore Norway (**?**). Fluid-flow simulations were computed by Norsk Hydro for the case of primary oil depletion from a horizontal well in the reservoir after 56 and 113 days of fluid production. For the purposes of this study, I will present only the results after 113 days of production compared to the initial reservoir state. Reservoir geology and core data measurements were combined to make rock physics transformations of the fluid-flow saturation, pressure and temperature data to seismic velocities and densities. Multi-offset elastic reflection seismogram surveys were simulated before and after the fluid depletion. Prestack migration images clearly show the location of gas coning after oil depletion for reasonable seismic noise levels, survey position errors and frequency bandwidth. Feasibility studies such as this may help reduce the financial risk associated with designing and implementing a seismic monitoring project given a pre-monitor engineering and petrophysical reservoir database.

1.3 Fluid-flow simulation

The reservoir used in this feasibility study is located within the Troll Field, which is a large oil and gas field offshore Norway in the North Sea. The oil zone is at a depth of approximately 1560 meters, and it varies in thickness from a few meters to more than 20 meters. Horizontal drilling technology makes it possible to commercially produce oil from this thin oil zone. A horizontal well penetrates the oil zone in the center of the simulation grid shown in Figure 1.3, and is perforated along the borehole for a length of about 500 hundred meters. Norsk Hydro provided fluid-flow simulations of primary oil production from this horizontal well before and after 113 days of oil depletion.

1.3.1 Reservoir properties

The productive interval of the reservoir consists of loosely consolidated sands with porosities ranging from 23% to 35%. Figure 1.1 shows the distribution of porosity in the reservoir on the simulation grid. All three fluid phases of oil, water and gas are simultaneously present. The reservoir oil is fairly heavy with a low gas-to-oil ratio of about 60. Typical values for the oil at reservoir conditions are: density 0.8 g/cc, bulk modulus 1020 MPa, viscosity 1.5 to 2.0 cp. The temperature in the reservoir is approximately uniform and remains constant at 60 $^{\circ}$C during oil depletion. The overburden pressure is approximately 34 MPa and the pore pressure remains approximately constant at about 16 MPa during depletion.

1.3.2 Simulation grid

The 2-D flow mesh consists of 312 individual blocks extracted from a larger 3-D simulation mesh, as schematically diagrammed in Figure 1.2. Figure 1.3 shows an

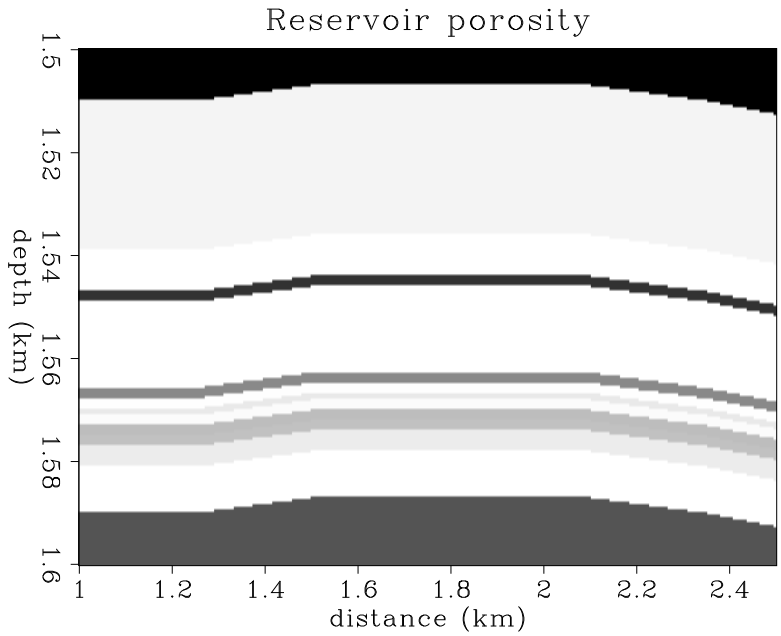

Figure 1.1: Porosity distribution in the reservoir, ranging from 23% (black) to 35% (white). feas-phi [ER]

expanded section of the reservoir grid in zone A. This irregular simulation grid ranges in depth intervals of one to tens of meters, and lateral intervals of tens to hundreds of meters. The grid covers a reservoir zone 45 m thick, comprised of 24 layers. The maximum structural dip along the reservoir is about 6° to the east (right side of figure), where the reservoir is truncated by 40 m of fault downthrow. At both simulation times of 0 and 113 days, each grid cell was loaded with a fluid-flow simulation data value of pore pressure, gas saturation, oil saturation, and water saturation. Temperature remained constant throughout the simulation.

1.3.3 Pore pressure

Pore pressure was calculated in the fluid-flow simulation after 113 days (Monitor 2) of oil production from the horizontal well, and at the initial Base survey state. The largest change in pore pressure during 113 days of simulated production is only -0.24 MPa (-35 psi), which is negligible in terms of velocity effect as shown in Figure 1.16. Figure 1.4 shows the change in pore pressure of the Monitor 2 simulation compared to the initial reservoir conditions. The diffusive decrease in reservoir pressure is associated with the withdrawal of oil from the vicinity of the horizontal wellbore, which is located at about 1560 m depth, and between 1.5–2.0 km distance in the coordinates of Figure 1.4. The heel of the well is located to the right, which explains the asymmetry of the pressure decrease during drawdown.

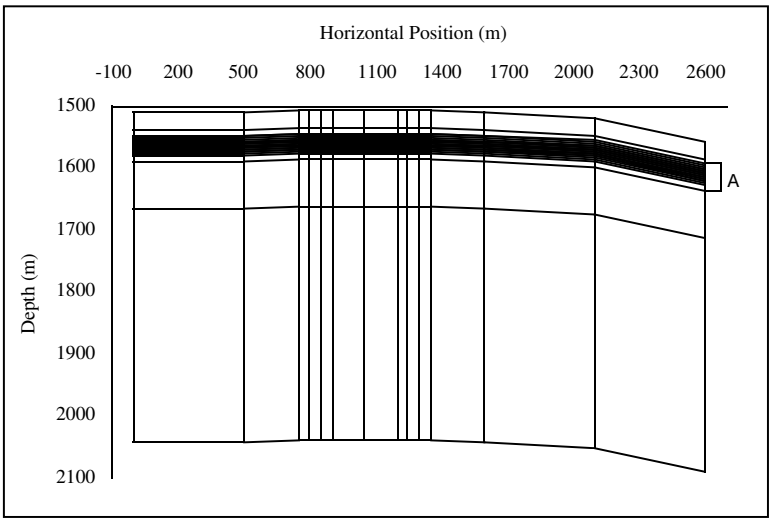

Figure 1.2: The reservoir fluid-flow simulation grid. Grid coordinates are shifted 750 m laterally compared to physical coordinates. feas-res-grid1 [NR]

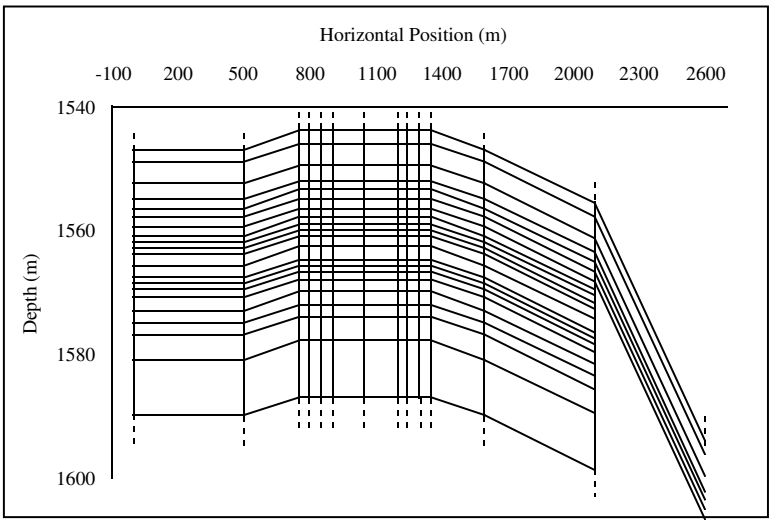

Figure 1.3: An expanded section "A" of the reservoir fluid-flow simulation grid. Grid coordinates are shifted 750 m laterally compared to physical coordinates. feas-res-grid2 [NR]

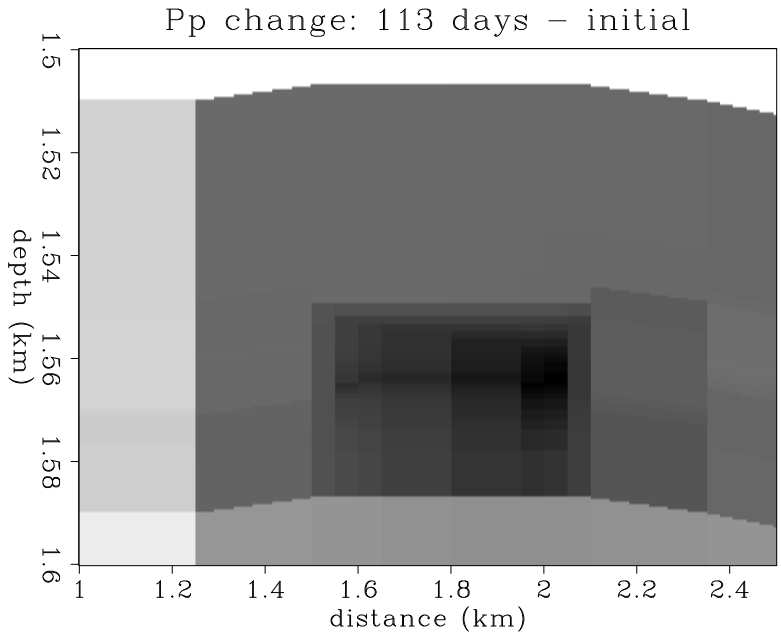

Figure 1.4: Pore pressure difference: 113 days − initial state. All pressure changes are negative. The maximum change is about −0.24 MPa (black). feas-pp31 [ER]

1.3.4 Oil saturation

Figure 1.5 shows the initial state of oil saturation in the reservoir. The main oil zone is about 20 m thick at a depth of 1560 m and has a maximum saturation value of 90%. Figure 1.6 shows the oil saturation distribution after 113 days of oil depletion. These plots show the oil zone being pinched out rapidly by gascap expansion from above, and aquifer upwelling from below. The pinch-out is indicative of a production rate that is too fast to maintain a stable oil zone.

1.3.5 Water saturation

Figure 1.7 shows the initial state of water saturation in the reservoir. A large aquifer underlays the oil zone, and the oil-water contact follows reservoir structure and porosity rather than a gravity fluid contact. Figure 1.8 shows the water saturation distribution after 113 days of oil depletion. Note the aquifer cresting upward in the center and the gravity sag at the flanks of the aquifer crest. The aquifer has crested upward near the horizontal wellbore to help displace oil into production. Gravitational forces cause a slight downwelling of the aquifer at the flanks to balance the upward cresting in the center.

1.3.6 Gas saturation

Figure 1.9 shows the initial state of gas saturation in the reservoir. A 50 m thick gascap overlays the oil zone, and is sealed at the top by an impermeable cap rock.

Figure 1.10 shows the gas saturation distribution after 113 days of oil depletion. Note the gascap coning downward in the center due to gas expansion associated with the reservoir pressure decrease. The gascap has coned downward near the horizontal wellbore to displace oil into production. Since the compressibility of gas is about two orders of magnitude larger than that of water (**?**), the gascap cones downward more than the aquifer cones upward. The significant amount of gascap expansion is the primary production drive mechanism for oil depletion in this reservoir. Since a large P-impedance contrast is associated with the gas zone, we hope to see a significant seismic response due to gascap coning, as is demonstrated later in this chapter.

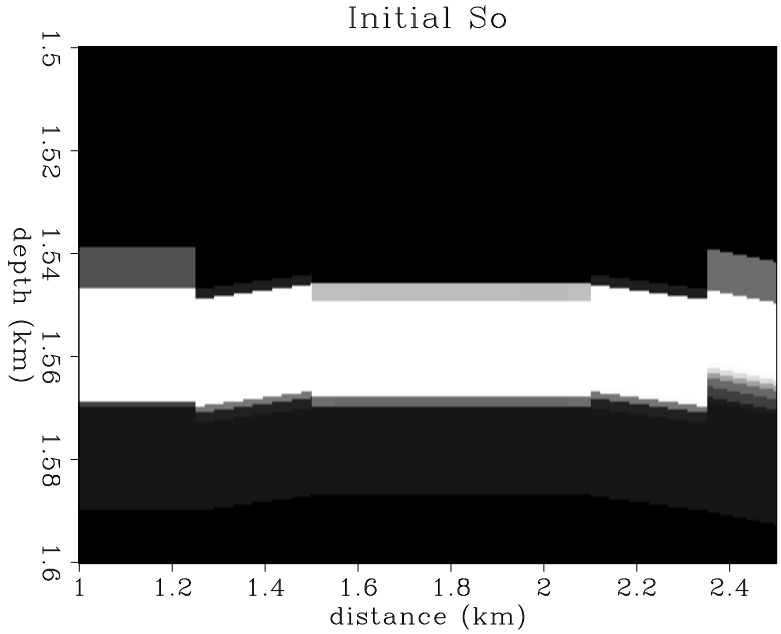

Figure 1.5: The initial oil saturation distribution. 100% saturation is white, 0% saturation is black. feas-so1 [ER]

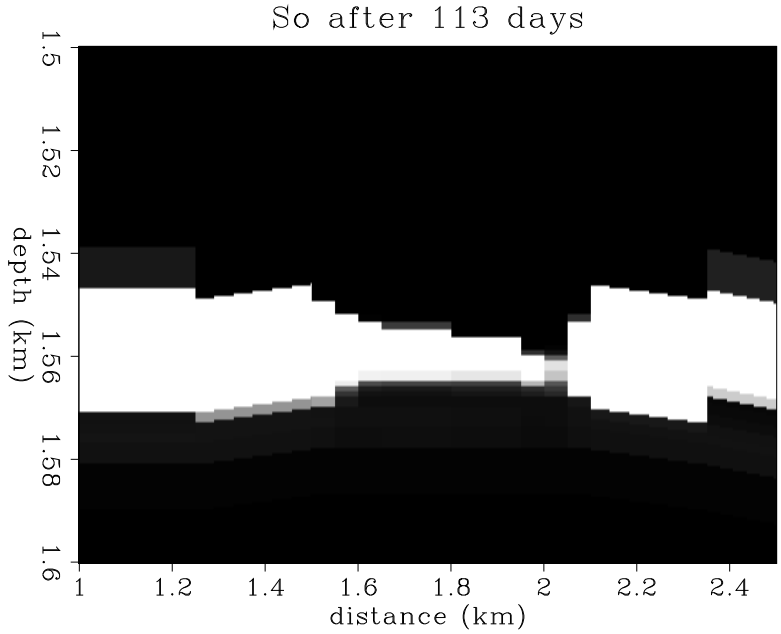

Figure 1.6: The oil saturation distribution after 113 days of production. 100% saturation is white, 0% saturation is black. feas-so3 [ER]

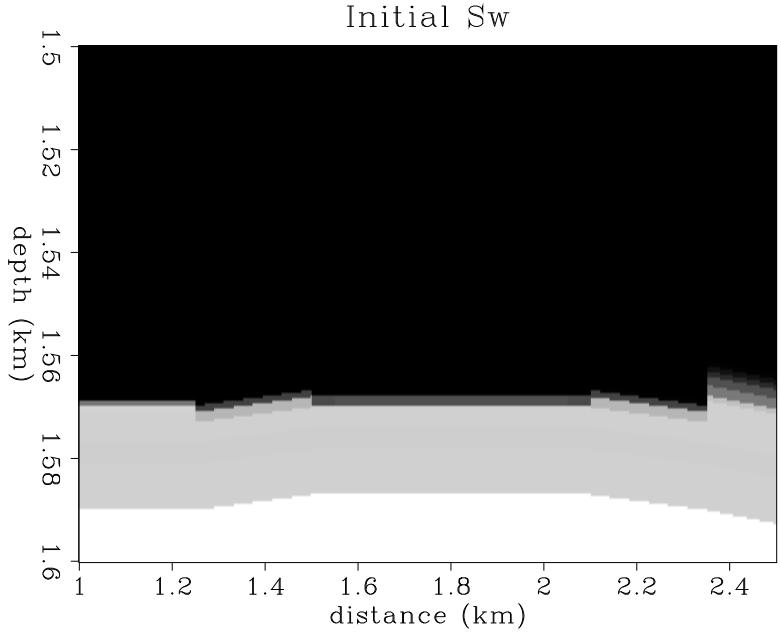

Figure 1.7: The initial water saturation distribution. 100% saturation is white, 0% saturation is black. feas-sw1 [ER]

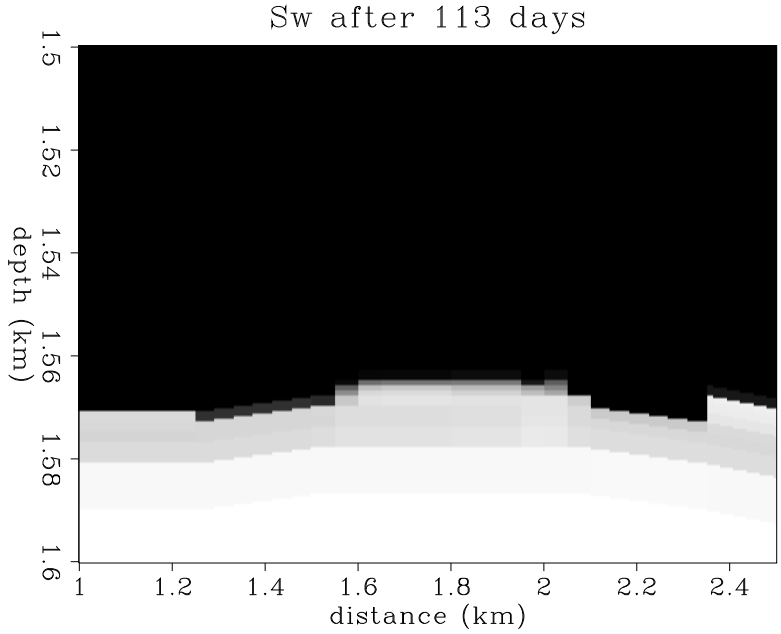

Figure 1.8: The water saturation distribution after 113 days of production. 100% saturation is white, 0% saturation is black. feas-sw3 [ER]

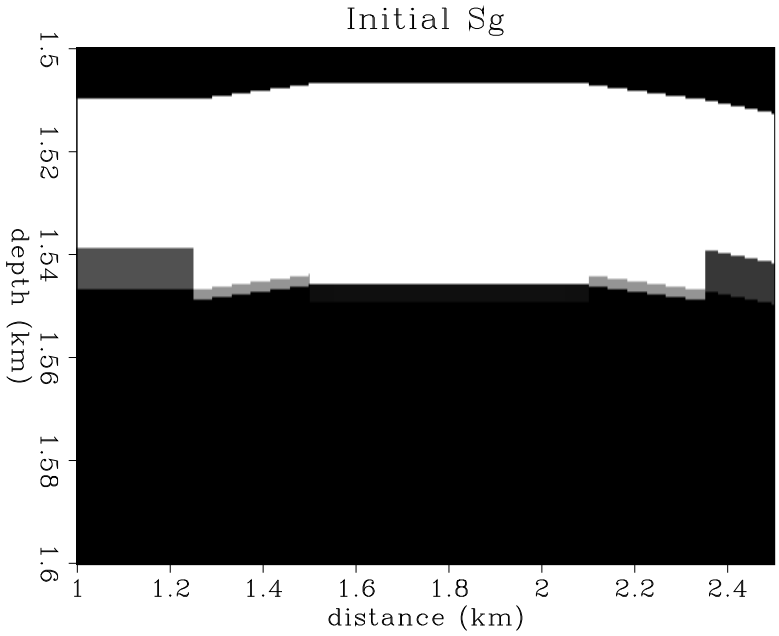

Figure 1.9: The initial gas saturation distribution. 100% saturation is white, 0% saturation is black. feas-sg1 [ER]

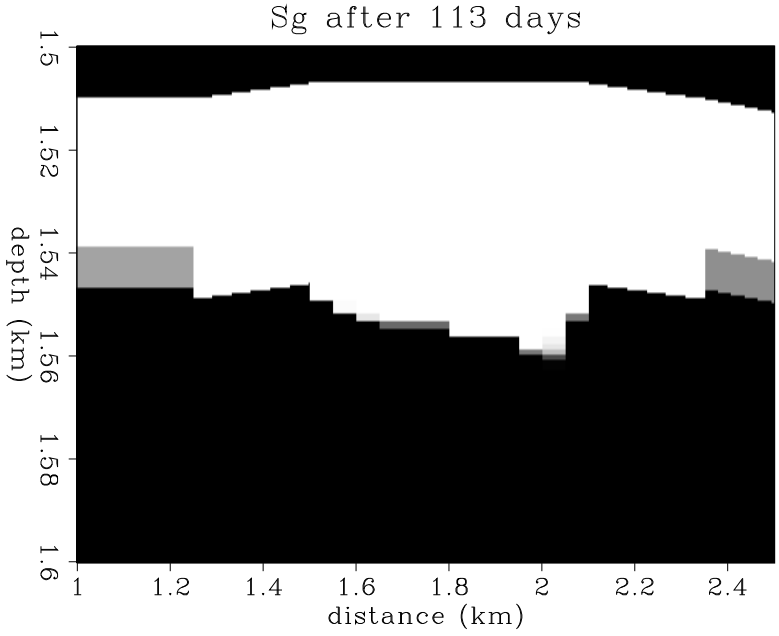

Figure 1.10: The gas saturation distribution after 113 days of production. 100% saturation is white, 0% saturation is black. feas-sg3 [ER]

1.4 Rock physics

Given the fluid-flow simulation data and reservoir geology description, rock physics analysis can be used to transform pressure, temperature and saturation data into P- and S-wave velocity $V_p = \alpha$ and $V_s = \beta$, and density distributions within the reservoir. First, the dry rock properties are estimated from laboratory core sample measurements as a function of mineralogy, porosity, pressure and temperature. Then, effective bulk moduli are computed for effective three-phase fluid mixtures of oil, gas and water, including the effects of temperature and pressure. Finally, saturated rock properties are calculated using Gassmann's equation to combine the dry-rock data and effective fluid moduli as a function of pressure, temperature, porosity, and fluid saturation.

1.4.1 Dry rock properties

Porosity effect

Estimates of dry rock properties in the reservoir are based on measurements from the Troll reservoir reported by Blangy and Strandenes (**?**) and Blangy (**?**), which involved laboratory experiments conducted on 38 core samples. In the reservoir sand, quartz is the dominant constituent, with volumetric content between 50% and 80%, feldspar content is almost constant at 20%, and mica volumetric content varies between 0% and 25%. Ultrasonic compressional and shear wave velocities were measured at varying differential hydrostatic stress from 5 to 30 MPa. Overburden pressure is approximately 34 MPa, pore pressure ranges around 16 MPa, resulting in a differential pressure of about 18 MPa. Therefore it is appropriate to select the core measurements of Blangy and Strandenes measured at a differential pressure of 20 MPa.

Figure 1.11 shows a scatter plot of the Blangy and Strandenes V_p core measurements made as a function of reservoir sand porosity at 20 MPa differential pressure. Figure 1.12 shows a similar scatter plot for V_s for varying porosities at 20 MPa differential pressure. The densities of the core samples have been computed based on their reported mineralogy volume fractions. The dry density values are plotted in Figure 1.13 at reservoir conditions. Based on the dry V_p, V_s and density data, the dry bulk moduli K_{dry} and dry shear moduli μ_{dry} of the 38 core samples was calculated using the relation:

$$K_{dry} = \rho(V_p^2 - \frac{4}{3}V_s^2) \quad ; \quad \mu_{dry} = \rho V_s^2 \ , \tag{1.1}$$

where ρ is the dry density. The results of the K_{dry} and μ_{dry} calculations are shown in Figures 1.14 and 1.15. The notation G for the shear modulus is identical to μ. A least-squares linear fit was made to the data with the result:

$$K_{dry} \approx 9357 - 16526\phi \ \ (\text{MPa}) \ , \tag{1.2}$$

and

$$\mu_{dry} \approx 11291 - 22840\phi \ \ (\text{MPa}) \,, \tag{1.3}$$

where the porosity ϕ ranges on a scale of 0.0–1.0. The standard deviation of the relative errors for each fit is about 10% for K_{dry} and 5% for μ_{dry}.

Pressure effect

Additionally, we need to know the properties of dry rocks with changing pore pressure. Han (**?**) made measurements on unconsolidated Ottawa sand (porosity 33%) that is structurally similar to many Troll reservoir rocks. Han measured dry V_p and V_s as a function of confining hydrostatic stress, which can be converted into velocity as a function of pore pressure, as shown in Figure 1.16. A similar plot shows the variation in velocity with temperature, but this is omitted since the reservoir under study does not change temperature during the simulated oil depletion.

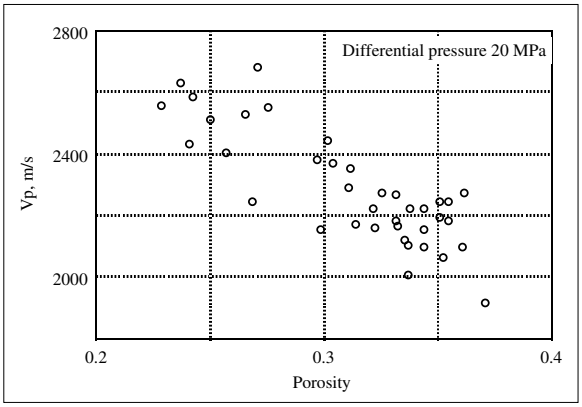

Figure 1.11: Dry V_p measured versus porosity at 20 MPa differential pressure (after Blangy and Strandenes, 1991). feas-vp-phi [NR]

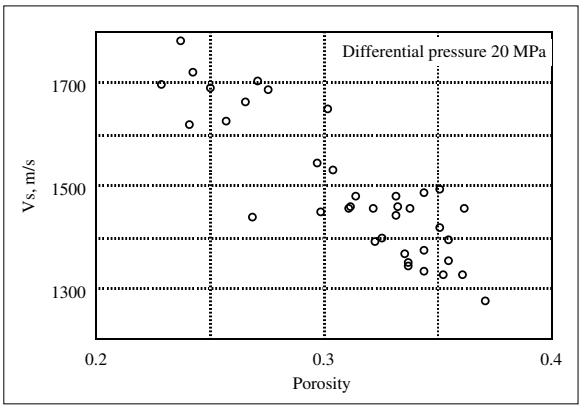

Figure 1.12: Dry V_s measured versus porosity at 20 MPa differential pressure (after Blangy and Strandenes, 1991). feas-vs-phi [NR]

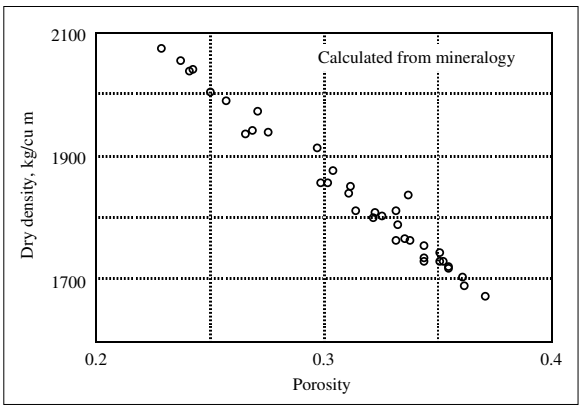

Figure 1.13: Dry density versus porosity calculated from mineralogy at reservoir conditions. feas-rho-phi [NR]

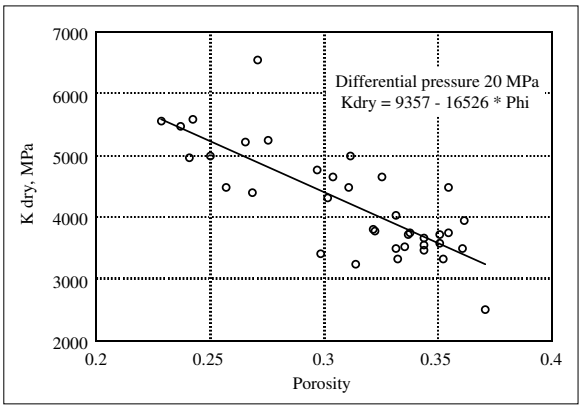

Figure 1.14: Dry bulk modulus K_{dry} calculated versus porosity at 20 MPa differential pressure. feas-kdry-phi [NR]

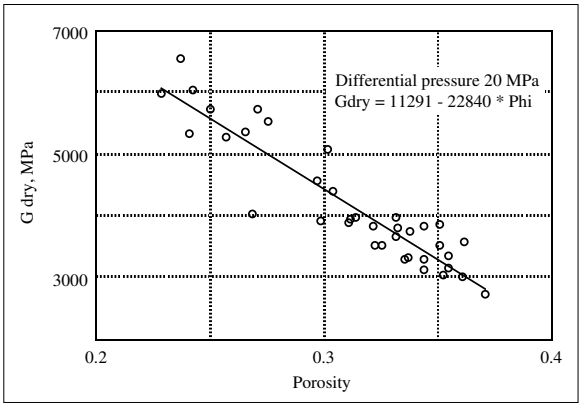

Figure 1.15: Dry shear modulus μ_{dry} calculated versus porosity at 20 MPa differential pressure. feas-gdry-phi [NR]

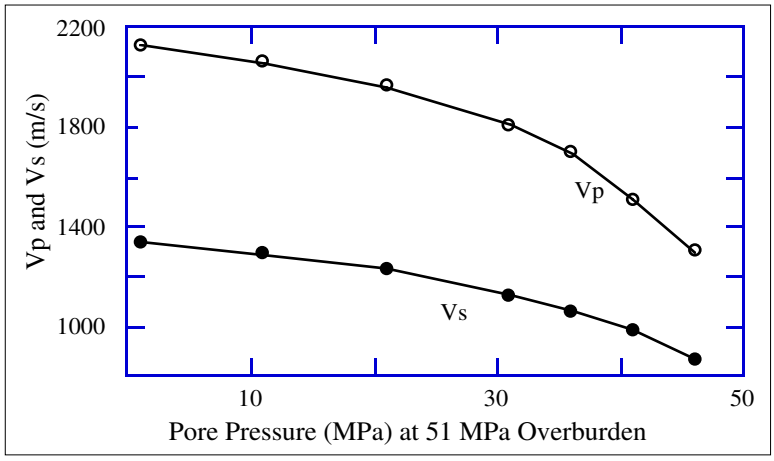

Figure 1.16: Compressional and shear wave velocities measured in dry Ottawa sandstone versus pore pressure at 51 MPa overburden pressure (after Han, 1986). feas-vpvs-pp [NR]

1.4.2 Saturated rock properties

The velocity effect of saturation can be calculated at seismic frequencies by using Gassmann's formulas (e.g., Bourbié et al., 1987). This formula relates the effective elastic moduli of a dry rock to the effective moduli of the same rock containing fluid, as discussed in Chapter 2:

$$\frac{K_{sat}}{K_{solid} - K_{sat}} = \frac{K_{dry}}{K_{solid} - K_{dry}} + \frac{K_{fluid}}{\phi(K_{solid} - K_{fluid})} , \tag{1.4}$$

and

$$\mu_{sat} = \mu_{dry} , \tag{1.5}$$

where K_{sat} and μ_{sat} are the effective bulk and shear moduli of the saturated rock. Gassmann's relations require knowledge of the effective shear and bulk moduli of the dry rock (μ_{dry} and K_{dry}), the bulk modulus of the mineral material making up the rock (K_{solid}), the effective bulk modulus of the saturating pore fluid (K_{fluid}), and the porosity ϕ. From Gassmann's formula I derive

$$K_{sat} = K_{solid} \frac{\phi K_{dry} - (1+\phi) K_{fluid} K_{dry}/K_{solid} + K_{fluid}}{(1-\phi) K_{fluid} + \phi K_{solid} - K_{fluid} K_{dry}/K_{solid}} \tag{1.6}$$

and use this last expression to compute the bulk modulus of saturated rock from dry data.

For partially saturated rocks at sufficiently low frequencies, an effective modulus K_{fluid} is used for the effective pore fluid, that is an isostress average of the moduli of the liquid and gaseous phases:

$$\frac{1}{K_{fluid}} = \frac{S}{K_{liquid}} + \frac{(1-S)}{K_{gas}} . \tag{1.7}$$

This requires knowledge of the bulk modulus of the liquid phase (K_{liquid}), the bulk modulus of the gas phase (K_{gas}), and the saturation values (S). In general, if the pore fluid includes more than two phases, the mixture's effective bulk modulus K_{fluid} is calculated based on the the number of fluid components N, the volumetric concentrations c_i of the ith component, and their bulk moduli K_i:

$$\frac{1}{K_{fluid}} = \sum_{i=1}^{N} \frac{c_i}{K_i} . \tag{1.8}$$

Finally, the following formulas are used to find seismic velocities in saturated rocks:

$$V_{p_{sat}} = \sqrt{\frac{(K_{sat} + \frac{4}{3}\mu_{sat})}{\rho_{sat}}} \tag{1.9}$$

and

$$V_{s_{sat}} = \sqrt{\frac{\mu_{sat}}{\rho_{sat}}} \ , \tag{1.10}$$

where ρ_{sat} is the density of the saturated rock:

$$\rho_{sat} = (1 - \phi)\rho_{solid} + \phi\rho_{fluid} \ , \tag{1.11}$$

ρ_{solid} is the density of the solid phase, and ρ_{fluid} is the density of the fluid mixture obtained as an arithmetic mean of the volume-concentration-weighted fluid density components ρ_i:

$$\rho_{fluid} = \sum_{i=1}^{N} c_i \rho_i \ . \tag{1.12}$$

The following typical values are assumed for the reservoir water: a density of 1.0 g/cc and a bulk modulus of 2250 MPa. This process allows us to calculate fluid properties that depend on fluid-flow saturation values. These properties will depend on pressure and temperature because the bulk modulus and density of the reservoir gas are affected by these two parameters. As an example, the pressure-dependent Ottawa sand P-wave velocity of Figure 1.16 can be converted to be dependent on both pressure and fluid saturation (oil, water or gas), as shown in Figure 1.17 (Dvorkin, pers. comm.).

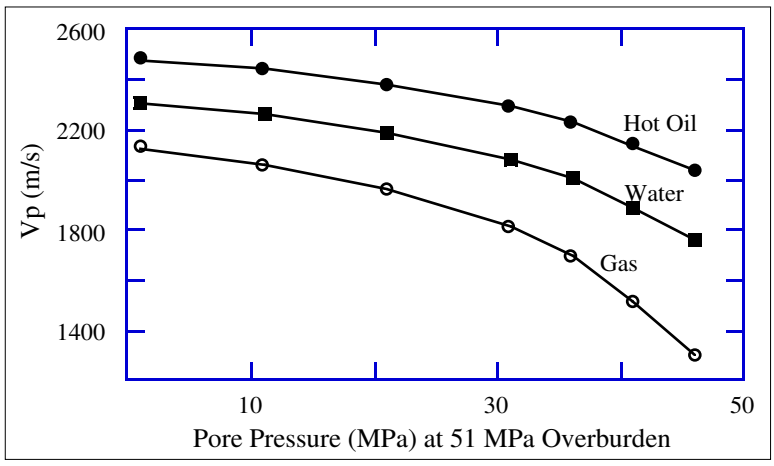

Figure 1.17: Compressional velocity in Ottawa sand as a function of pore pressure and oil/water/gas saturation (Dvorkin, pers. comm.). feas-vp-pp-sat [NR]

1.4.3 Pressure-dependent gas properties

Pressure- and temperature-dependent gas properties are calculated using the method of Batzle and Wang (**?**), as follows. The reservoir gas is assumed to be primarily methane, which has a specific gravity of 0.55 compared to air. Pseudo-reduced pressure and temperature are related to reservoir pore pressure and temperature as:

$$P_{pr} = \frac{P}{(4.892 - 0.4048\ G)}\ , \tag{1.13}$$

and

$$T_{pr} = \frac{T_a}{(94.72 + 170.75\ G)}\ , \tag{1.14}$$

where G is the gas specific gravity, T_a is absolute temperature: $T_a = \ ^{\circ}C + 273$. The pressure is given in MPa. Gas density is

$$\rho_{gas} \approx \frac{28.8\ GP}{ZRT_a}\ , \tag{1.15}$$

where the "Z-factor" is defined as:

$$Z = [0.03 + 0.00527(3.5 - T_{pr})^3]\ P_{pr} + (0.642\ T_{pr} - 0.007\ T_{pr}^4 - 0.52) + E\ , \tag{1.16}$$

and

$$E = 0.109(3.85 - T_{pr})^2\ e^{-\alpha}\ , \tag{1.17}$$

$$\alpha = [0.45 + 8(0.56 - T_{pr}^{-1})^2]\ P_{pr}^{1.2}\ T_{pr}^{-1} \tag{1.18}$$

and $R = 8.31$ is the universal gas constant. For an ideal gas, the Z-factor is equal to unity in the generalized Gas Law $PV = ZnRT$. For non-ideal gases, Z rarely varies beyond the range (0.5, 5.0).

The adiabatic gas bulk modulus K_s is:

$$K_s \approx \frac{P\gamma_0}{\left(1 - \frac{P_{pr}}{Z}\frac{\partial Z}{\partial P_{pr}}\right)_T} \tag{1.19}$$

where

$$\gamma_0 = 0.85 + \frac{5.6}{P_{pr} + 2} + \frac{27.1}{(P_{pr} + 3.5)^2} - 8.7\ e^{-0.65(P_{pr}+1)}\ , \tag{1.20}$$

and $(\partial Z/\partial P_{pr})$ can be calculated from Equation (1.16) for Z.

This rock physics analysis allows us to calculate seismic velocities in saturated reservoir rock as a function of mineralogy, fluid type and saturation value, pore pressure and temperature. Therefore, P-wave and S-wave velocity and density can be mapped as a function of the reservoir grid directly from the fluid-flow simulation values of pressure, temperature, and oil, gas and water saturation.

1.4.4 P-wave velocity

Figure 1.18 shows the initial V_p velocity distribution, which is largely dominated by the porosity before oil depletion. Velocities range from 2.1 km/s (dark gray) to 3.3 km/s (white). Figure 1.19 shows the V_p distribution after 113 days of oil depletion. A V_p decrease from about 2.5 to 2.1 km/s is evident in the area that the gascap is expanding downward, which is due largely to gas replacing oil in the pore space. Figure 1.20 shows the change in V_p after 113 days of oil depletion. There is a -400 m/s decrease in V_p in the gas cone, and a smaller $+100$ m/s increase in V_p where the aquifer has crested upward from below allowing water to displace oil.

Density variations in the reservoir are of the same polarity as the V_p variations. Density decreases from about 2.1 g/cc to 1.8 g/cc in the gas cone, and increases to about 2.15 g/cc in the water crest. Because the density plots look qualitatively similar to the V_p plots, they have been omitted here for brevity.

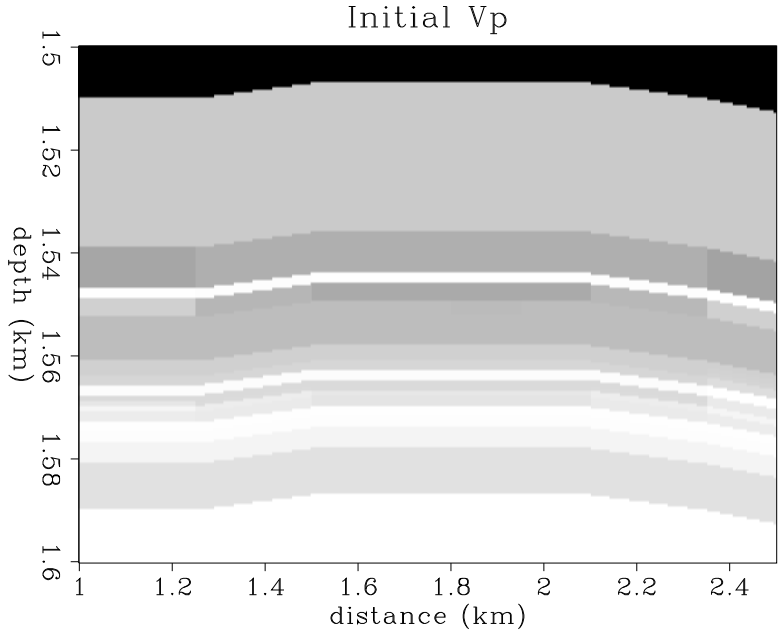

Figure 1.18: The initial V_p distribution. Velocities range from 2.1 km/s (dark gray) to 3.3 km/s (white). feas-vp1 [ER]

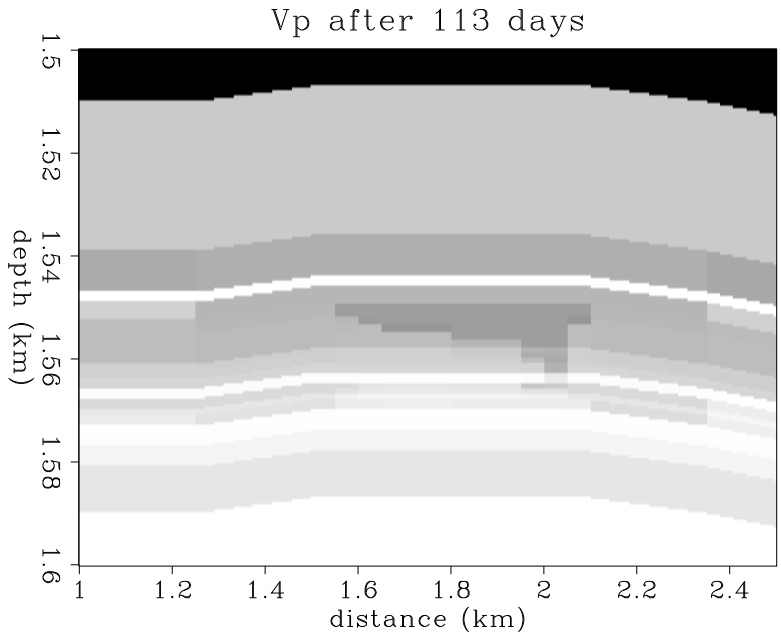

Figure 1.19: The V_p distribution after 113 days of production. Velocities range from 2.1 km/s (dark gray) to 3.3 km/s (white). feas-vp3 [ER]

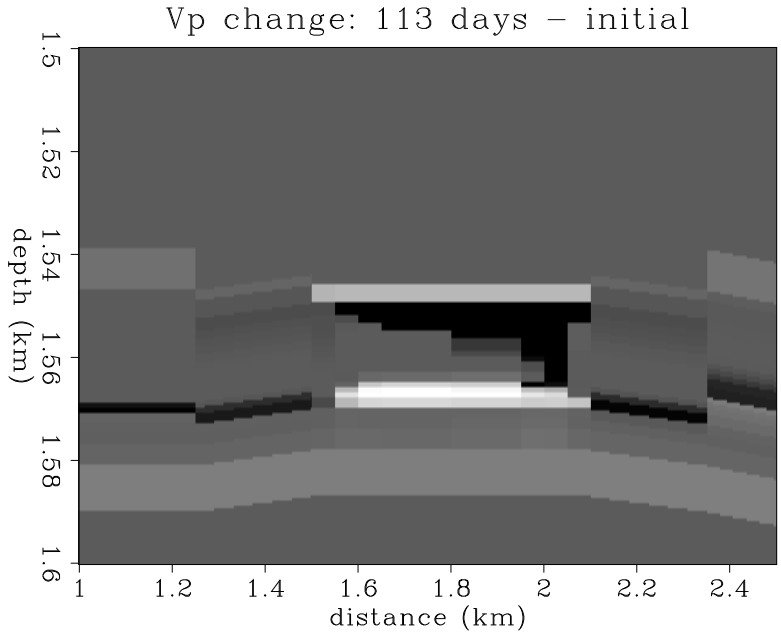

Figure 1.20: The change in V_p: 113 days – initial state. +140 m/s is white, −400 m/s is black. feas-vp31 [ER]

1.4.5 S-wave velocity

Figure 1.21 shows the initial V_s velocity variation, caused mostly by initial porosity variations. Velocities range from 1.2 km/s (dark gray) to 2.0 km/s (white). Figure 1.22 shows the V_s distribution after 113 days of oil depletion. A V_s increase from about 1.5 to 1.6 km/s is evident in the area that the gascap is expanding downward, which is due to the density decrease of gas replacing oil in the pore space. Since the pore pressure change is too small to affect μ_{dry} much, and fluid saturation does not affect the shear modulus at all according to Gassmann's equations (1.5), the decrease in density due to gas replacing oil must therefore cause an increase in V_s. Figure 1.23 shows the change in V_s after 113 days of oil depletion. There is a +80 m/s increase in V_s in the gas cone, and a smaller -20 m/s decrease in V_s where the aquifer has crested upward from below allowing water to displace oil.

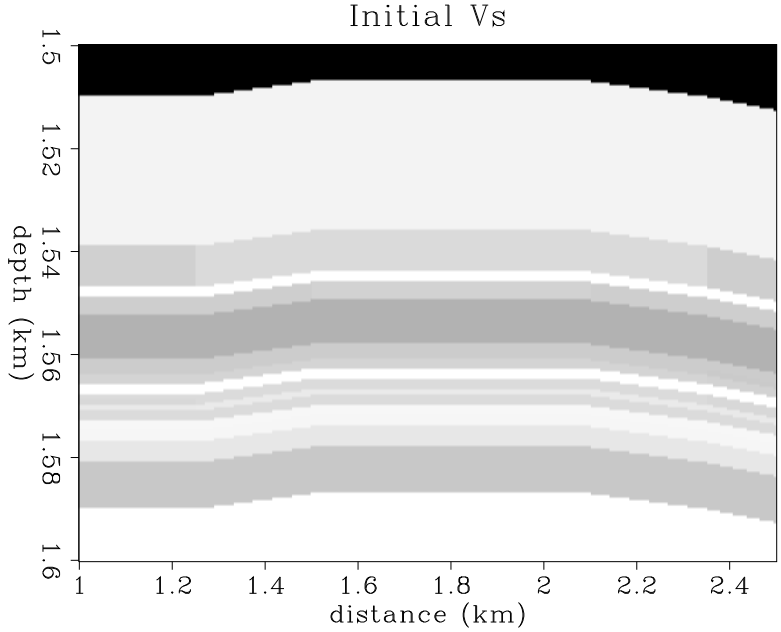

Figure 1.21: The initial V_s distribution. Velocities range from 1.2 km/s (dark gray) to 2.0 km/s (white). feas-vs1 [ER]

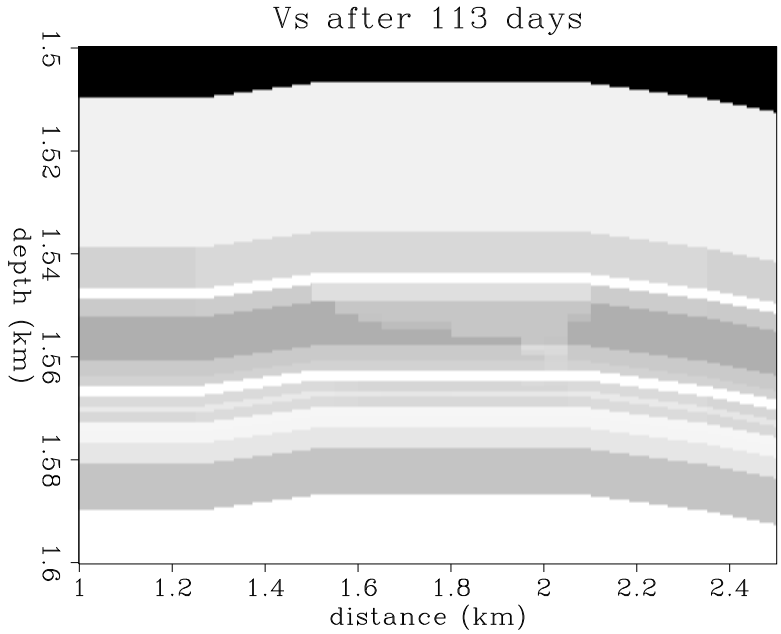

Figure 1.22: The V_s distribution after 113 days of production. Velocities range from 1.2 km/s (dark gray) to 2.0 km/s (white). feas-vs3 [ER]

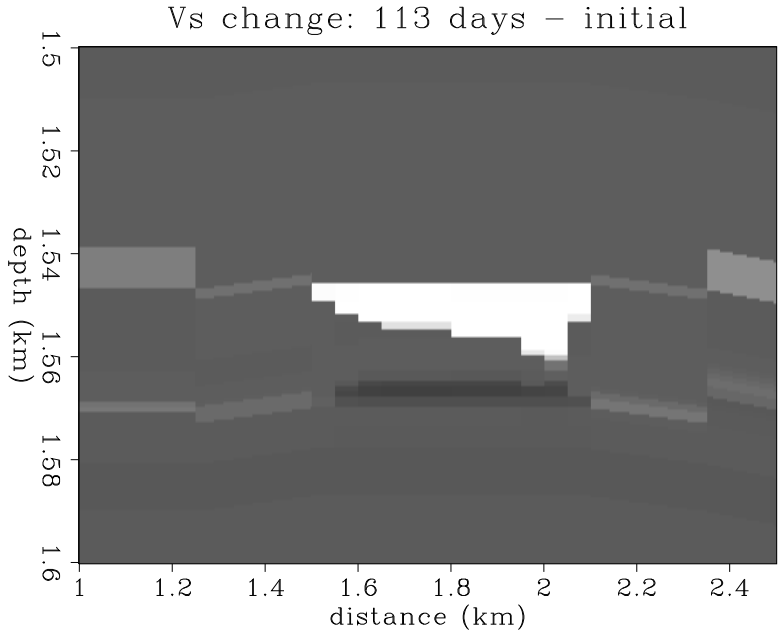

Figure 1.23: The change in V_s: 113 days – initial state. +80 m/s is white, −20 m/s is black. feas-vs31 [ER]

1.5 Seismic monitoring analysis

This section of the chapter deals with the seismic monitoring analysis of the Troll reservoir in simulated production. In particular, I discuss the total seismic model construction, and upscaling of fine-scale reservoir properties to an equivalent seismic-scale reservoir model for seismogram calculation. I use a Kirchhoff reflectivity method to simulate a prestack surface seismic survey before and after oil depletion in the reservoir. These two prestack datasets were then processed to produce stacked and prestack-migrated reflectivity images. Difference images obtained by subtracting combinations of stacked and migrated sections clearly show that reservoir fluid movement is visible in the seismic data and can be monitored in the presence of reasonable levels of seismic noise and survey errors.

1.5.1 Troll seismic model

A total seismic model of P- and S-wave velocity and density was constructed based on information provided by Norsk Hydro, as shown in Figure 1.24. The total model consists of a 1-D "overburden" macro-model merged with a 2-D fine-scale reservoir model.

A vertically-stratified "overburden" model was designed to optimize intensive synthetic seismogram computation while still preserving the overall character of the stacked section and the simple v(z) interval velocity model provided by Norsk Hydro. The macro-layers of the overburden model were chosen to approximate the position and relative reflection amplitude of reflectors seen in a Norsk Hydro stacked section at the well location. The well penetrates the reservoir horizontally at about 1.55 km depth at the 1.5–2.0 km midpoint distance in the coordinate system shown in Figure 1.24.

Curves of V_p, V_s and density are shown at the well location as a function of depth in Figure 1.25. The 1-D overburden increases slowly with depth down to the top of the reservoir, with a slight low velocity zone in the middle of depth section. The reservoir zone at 1.55 km depth has a strong low velocity and density contrast due to the gas cap, and then increases to a regional profile at and below the base of the reservoir.

1.5.2 Upscaled reservoir model

Figure 1.27 shows a fine-layered model of P-impedance calculated from the fluid-flow simulations provided by Norsk Hydro. The fine-scale seismic properties were mapped from reservoir pressure, temperature, relative saturation values of oil, water and gas, and porosity as described by the previous rock physics section of this chapter.

An issue of upscaling arises because in situ reservoir properties measured at very small spatial scales are not necessarily the same properties that a seismic wavefield

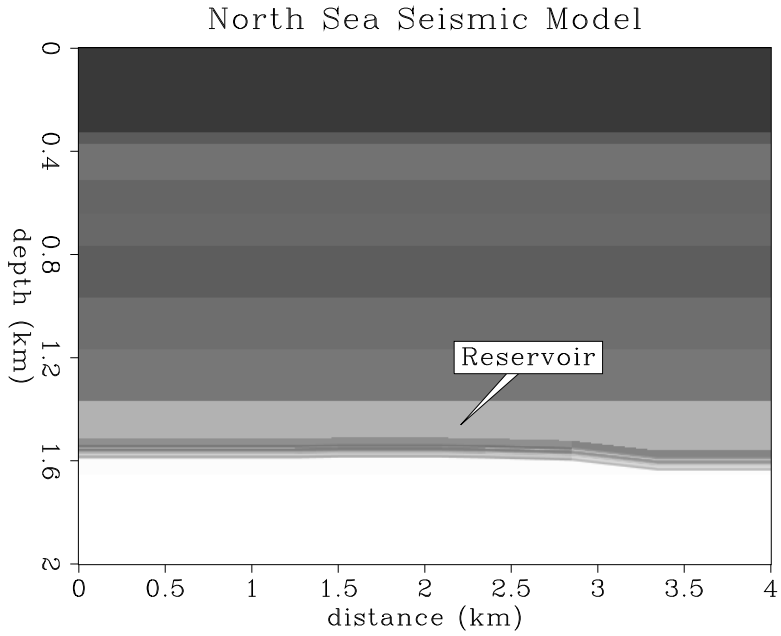

Figure 1.24: P-wave velocity model consisting of a 1-D "overburden" structure and a 2-D fine-layered reservoir zone at 1.5–1.6 km depth. feas-Vp1-ann [ER]

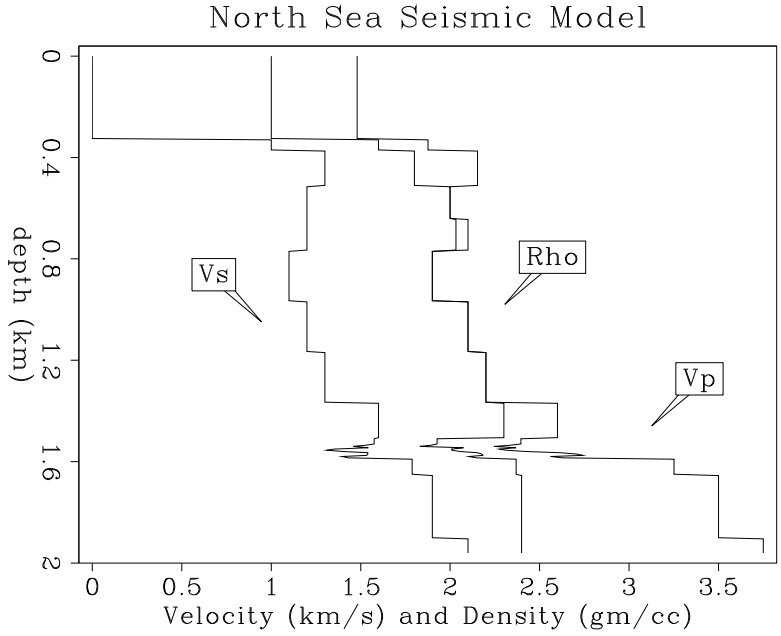

Figure 1.25: Initial velocity and density curves at the surface well position (2 km). feas-curves0-ann [ER]

samples at larger seismic wavelength scales. The reservoir simulation used a grid mesh that represented fine-layering on a scale as small as 1 meter in thickness. It might be computationally prohibitive to compute prestack seismograms on a mesh that small, and may not be physically meaningful even if one could do so, since modeling assumptions of spatial smoothness in properties may be violated at the fine scale (e.g., finite-difference derivatives could be inaccurate on the fine mesh).

Instead, I consider an "equivalent medium" sampled on a coarse mesh that propagates seismic wavefields which are dynamically equivalent to the waves that would have propagated in the true fine-layered medium. This equivalent medium can be approximated by a volume-weighted average of elastic compliance and density which attempts to conserve the stress-strain energy of elastic waves and the mass density of the medium, Schoenberg and Muir (**?**); Muir et al. (**?**).

The upscaling was done as follows. First, an over-sampled representation of the fine scale reservoir model was obtained at a sampling interval of 0.5 m in depth and 2.5 m in midpoint distance. Next, the equivalent medium averaging was done for isotropic elastic P and S compliances and density onto a coarse mesh of 5 m by 5 m in depth and midpoint. The upscaled compliances were then converted to P- and S-impedance to give the final upscaled seismic models at a mesh interval that is about one tenth of a seismic wavelength, as opposed to the original 1/100th of a seismic wavelength.

Figure 1.26 shows the fine-scale and upscaled V_p, V_s and density curves in the reservoir at the wellbore location. Figure 1.28 shows the upscaled coarse-mesh equivalent reservoir model of P-impedance. Similar upscaled equivalent models were calculated for S-impedance and density.

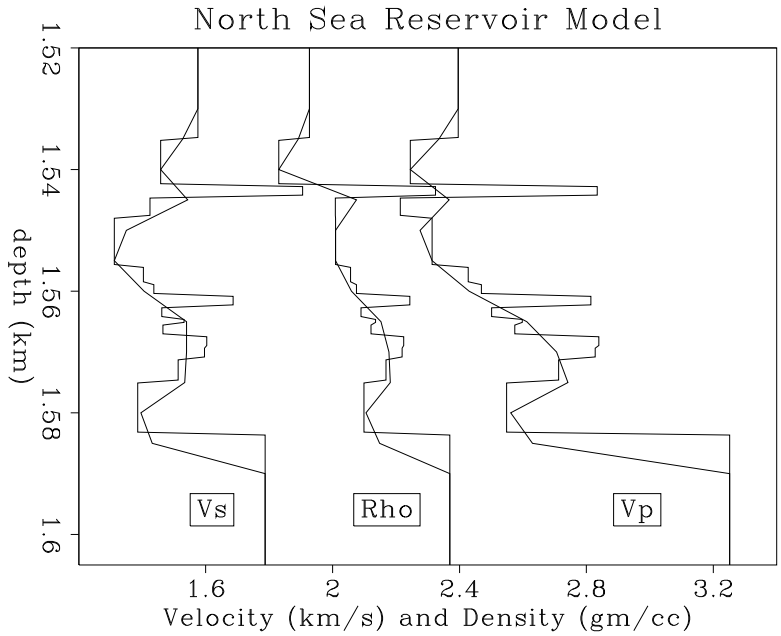

Figure 1.26: Reservoir velocity and density model curves. Blocky curves are fine-mesh values at 0.5 m depth intervals, smooth curves are equivalent upscaled values at 5 m intervals. feas-bgcurves-ann [ER]

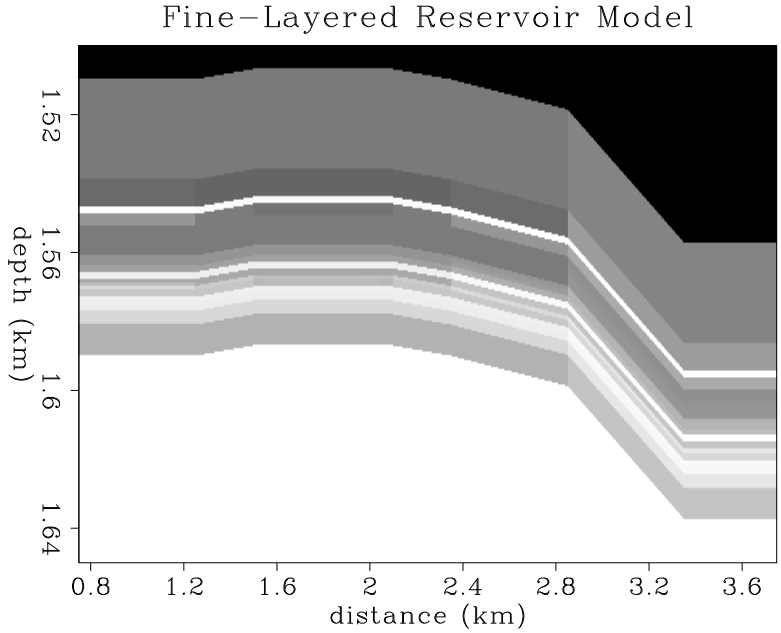

Figure 1.27: P-impedance reservoir model evaluated on a fine grid mesh. feas-res1 [ER]

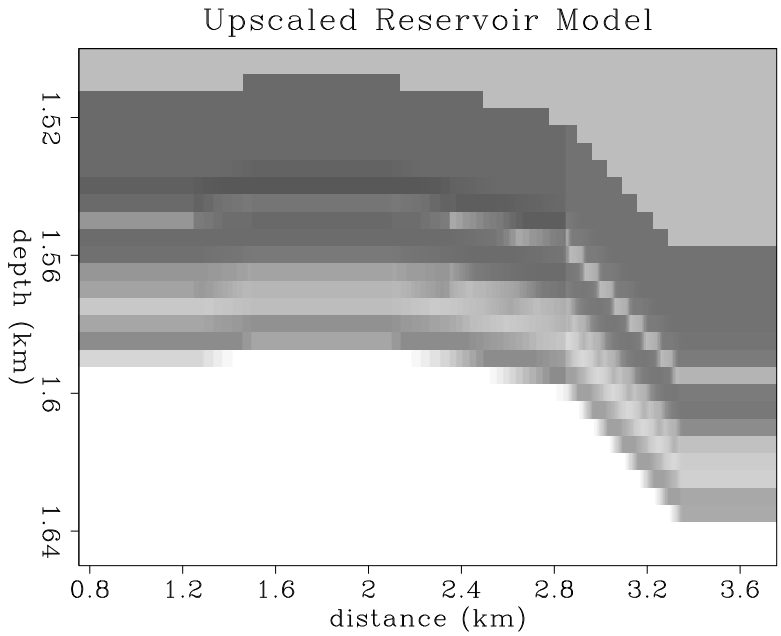

Figure 1.28: Upscaled P-impedance reservoir model on a coarse grid mesh. Obtained by averaging elastic compliances and density from fine to coarse mesh scales. feas-res2 [ER]

1.5.3 Time-variant seismic models

Using the equivalent medium upscaling procedure described above, P- and S-impedance, and density models were computed for both of the production monitoring phases. The monitors simulate fluid flow in the reservoir due to production in a horizontal well after zero and 113 days of production. For simplicity, I name the pre-depletion simulation as the "baseline survey", and the subsequent 113-day monitor as "monitor 2".

P-impedance

Figure 1.29 shows the initial state of seismic P-impedance (I_p). Figure 1.30 shows the I_p distribution after 113 days of oil depletion. In the vicinity of the wellbore, an asymmetric decrease in P-impedance is evident during production. This decrease in P-impedance is more clearly shown at 2 km in the curves of Figure 1.31. The decrease in P-impedance is due to downward coning and expansion of the gas cap to replace oil with gas near the wellbore. The coning asymmetry is probably due to lateral increase in flow pressure closest to the heel of the horizontal well. After the 113 days of depletion, the P-impedance decreases in the reservoir by a maximum relative contrast of about 15%, and is spread over a zone that is approximately 500 m wide and 15 m thick. This change in P-impedance will be shown later to cause a significant seismic reflection response.

S-impedance

Figure 1.32 shows the initial state of seismic S-impedance (I_s). Figure 1.33 shows the I_s distribution after 113 days of oil depletion. Barely any change in S-impedance is

visible in the zone of gas coning. This is because the shear modulus is not sensitive to fluid-saturation changes, and the pressure effect is also negligible at these small drawdown pore pressure changes. V_s has slightly increased due to a small decrease in density, and these two effects tend to cancel each other for S-impedance, which is the product of V_s and density. Thus, the overall result is a slight decrease in shear impedance during oil-replacement by expanding gas during production. The S-impedance curves of Figure 1.34 at the well location show that the S-impedance decreases a maximum of 5% at the cone, but is more representatively a decrease of about 2% spread over the entire zone of gas coning.

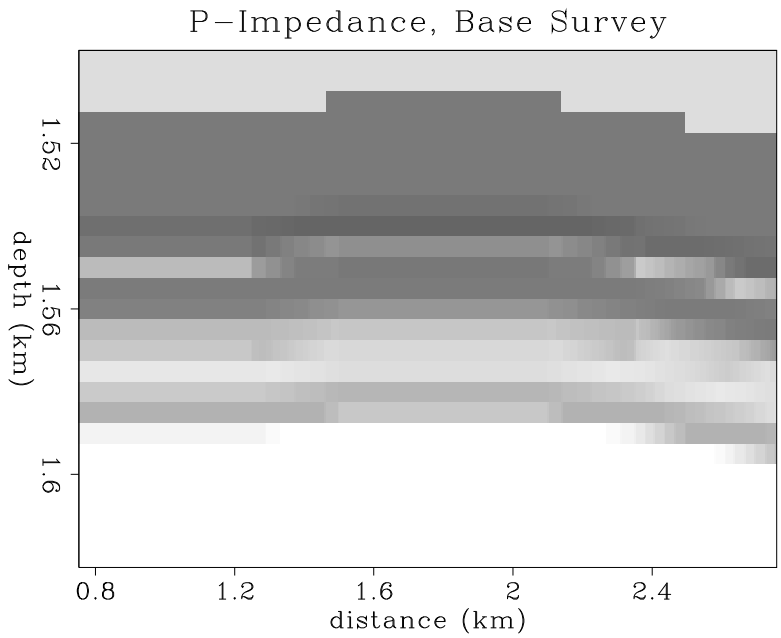

Figure 1.29: Initial P-impedance distribution in enlarged reservoir zone. I_p ranges from 3.8 (dark gray) to 7.8 km/s-g/cc (white). feas-ip1 [ER]

1.5.4 Kirchhoff seismogram modeling

Given the reservoir models before and after oil depletion, synthetic surface reflection seismic data can be generated for each time snapshot of production.

The synthetic seismograms are calculated based on the generalized Kirchhoff body force scattering theory of Lumley and Beydoun (**?**). This theory combines Zoeppritz plane-wave reflection and Rayleigh-Sommerfeld elastic diffraction responses. The modeling theory can generate the correct AVO response for locally planar reflectors, and merge into diffraction where elastic properties vary spatially faster than a seismic wavelength. However, since the Green's tensors are WKBJ ray-valid, only primary reflections and diffractions are computed. Higher order multiple scattering or phenomena such as surface waves are not modeled.

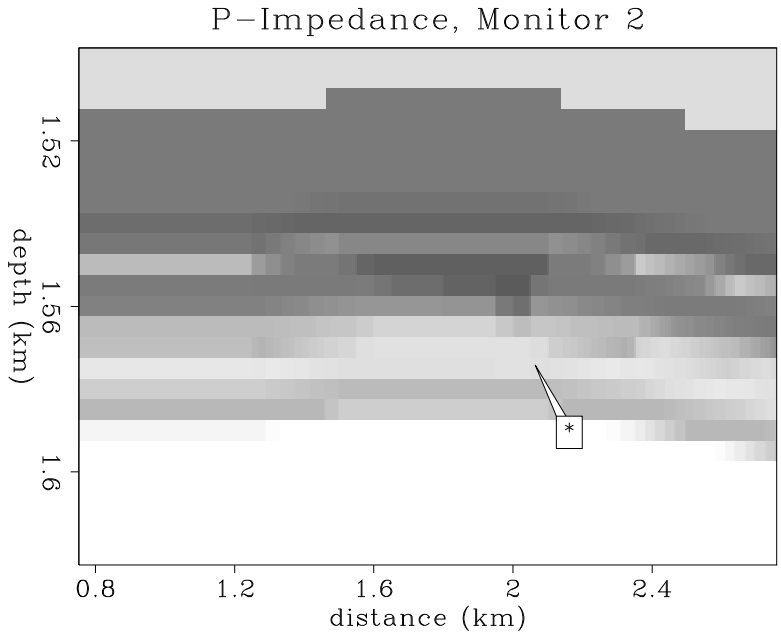

Figure 1.30: P-impedance distribution after 113 days of oil production. The averaged I_p values have decreased by about 15% in the production interval. feas-ip3-ann [ER]

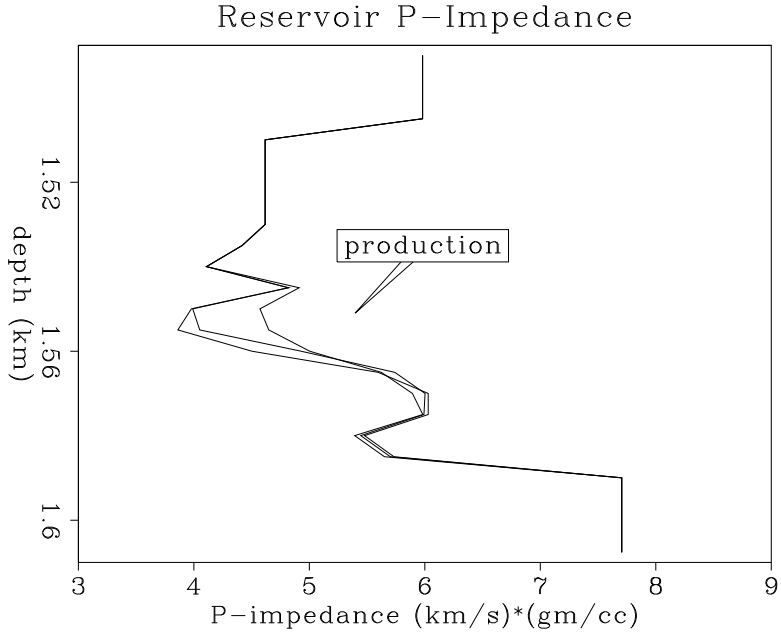

Figure 1.31: Reservoir time-varying P-impedance curves. Averaged P-impedance decreases significantly by about 10–15% with increasing production time due to gas coning. feas-ipcurves-ann [ER]

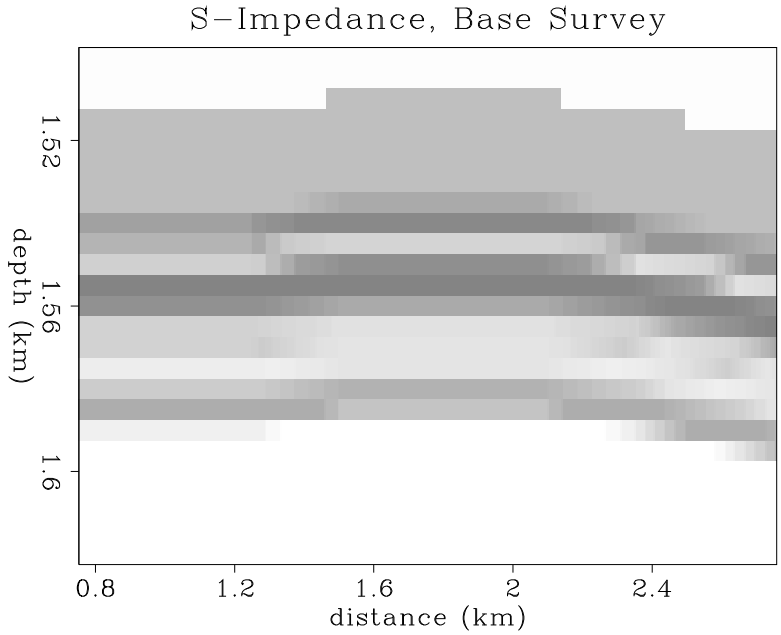

Figure 1.32: Initial S-impedance distribution in enlarged reservoir zone. I_s ranges from 2.5 (dark gray) to 4.2 km/s-g/cc (white). feas-is1 [ER]

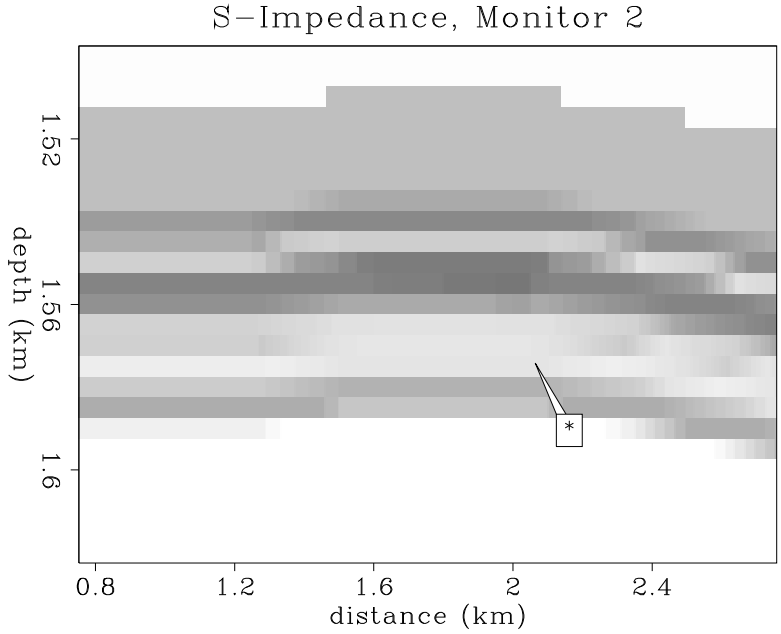

Figure 1.33: S-impedance distribution after 113 days of oil production. The averaged I_s values have decreased by about 5% in the production interval. feas-is3-ann [ER]

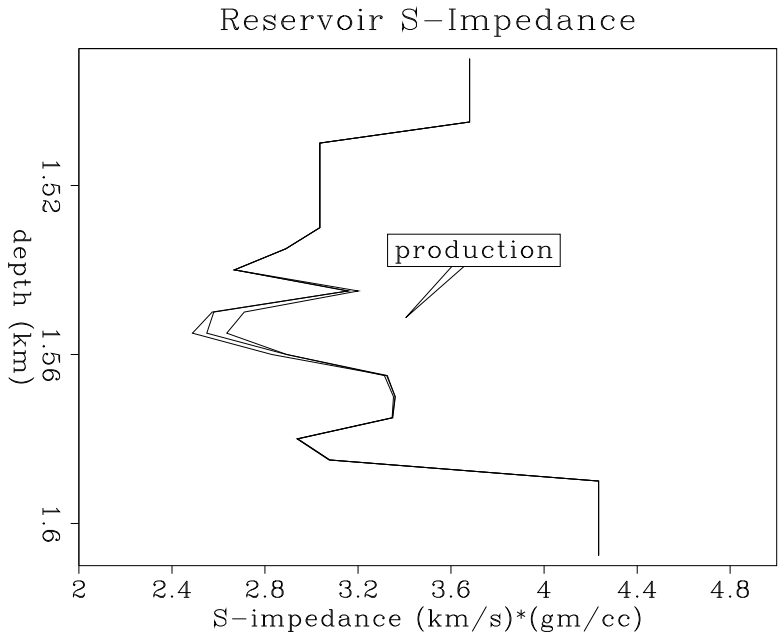

Figure 1.34: Reservoir time-varying S-impedance curves. S-impedance decreases slightly by about 2–5% with increasing production time due to gas coning. feas-iscurves-ann [ER]

The modeling theory is based on a volume integration of the body force equivalent of the $\grave{P}\acute{P}$ coefficient:

$$\hat{\mathbf{a}}_r \cdot \mathbf{u}^P(\mathbf{x}_r) = \int_{\mathcal{V}} ik\, A_s A_r e^{i\omega\tau_{sr}} \grave{P}\acute{P} \cos\phi_r \, d\mathcal{V} \ . \tag{1.21}$$

$\mathbf{u}^P$ is the P-P scattered vector wavefield measured at the receiver position $\mathbf{x}_r$, and projected onto an arbitrary receiver component direction $\hat{\mathbf{a}}_r$. A_s and A_r are the elastic WKBJ Green's function amplitudes from the source and receiver positions respectively, to each subsurface scattering point $\mathbf{x}$ in the volume $\mathcal{V}$. Similarly, $\tau_{sr} = \tau_s + \tau_r$ is the total traveltime from source to scatterer to receiver. The factor $\cos\phi_r$ is the non-geometric diffraction angle as shown in Figure 1.35, and is unity along the Snell reflection path (specular), and variable otherwise. The $\grave{P}\acute{P}$ factor is the plane-wave Zoeppritz elastic P-P reflection coefficient, and k is the spatial wavenumber $k = \omega/\alpha$. The incident arrival direction vector $\hat{\mathbf{t}}^P$ is drawn in Figure 1.35.

The volume integration gives the impulse response seismograms which can then be filtered to any desired bandwidth and convolved with a wavelet. Additionally, spatially-uncorrelated Gaussian distributed noise, filtered to match the same frequency bandwidth as the seismic signal, may also be added to produce fairly realistic primary reflection data with accurate AVO responses and the presence of seismic noise.

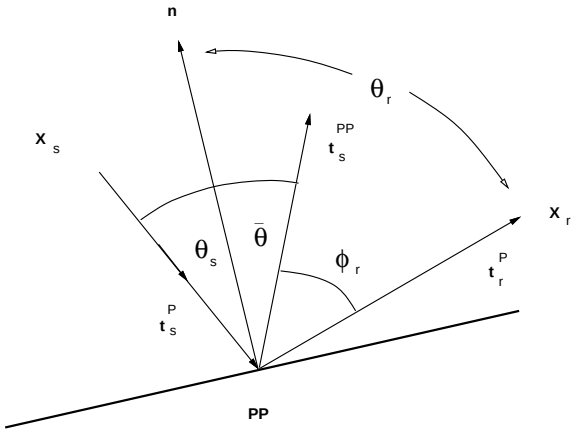

Figure 1.35: Generalized Kirchhoff reflection and diffraction angle geometries. feas-anglegeom [NR]

1.5.5 CMP gather analysis

Synthetic seismograms were generated at the CMP location directly above maximum coning, at 2 km distance in the midpoint coordinate. A typical marine acquisition geometry of 60-fold CMP gathers was simulated with a near offset of 250 m and a 3 km cable length. The bandwidth of the seismic data have corner frequencies of 5, 10, 60 and 80 Hz. Random spatially-uncorrelated Gaussian noise was filtered to the same bandwidth and added to make the "noisy" seismic traces. The signal-to-noise (S/N) amplitude ratio is about 2:1 at the main reservoir reflections at 1.6 seconds. For display purposes, the CMP gathers have been divergence-corrected and compensated for source-receiver amplitude directivity.

Figure 1.36 shows a close-up of the reservoir reflections in the noise-free CMP gather at the time of the baseline survey (left panel), and after 113 days of oil depletion (right panel). Figure 1.37 shows the same CMP gathers but with added noise. The top of the reservoir is the first negative reflection at about 1.55 seconds, and the complex wavetrain following is due to the fine-layered nature of the reservoir zone. Since the velocity increases from the top to the bottom of the reservoir, the clean reservoir reflections tend to coalesce into one single low-frequency high-amplitude waveform at far offsets.

The CMP gathers after 113 days of oil depletion (right panel) show some changes with respect to the baseline CMP gathers (left panel). Due to the decrease in P-impedance at the gas cone, the negative reflection at 1.6 seconds, slightly below the top of the reservoir, has increased in magnitude, as has its positive side-lobe at about 1.61 seconds. This gives the near offset waveforms a "doublet" character after oil depletion. There is also an apparent increase in wavetrain amplitude with offset, compared to the baseline survey CMP gathers. The increased near-offset reflection amplitude and change in waveform character are visible in the clean and noisy data. The AVO increase is visible in the clean CMP gathers, but partially obscured by noise in the noisy gathers.

Figure 1.38 shows the "difference gathers" obtained by subtracting the CMP gathers of the baseline survey from those after 113 days of oil depletion. A single Hilbert-shaped diffraction waveform expresses the difference between the two surveys. The dipole Hilbert shape arises from a negative P-impedance contrast at the top of the gas cone, followed closely by an increase in P-impedance in the unchanged reservoir at the base of the cone. The difference diffraction is visible in the noisy data with a S/N ratio of about 1.5:1.

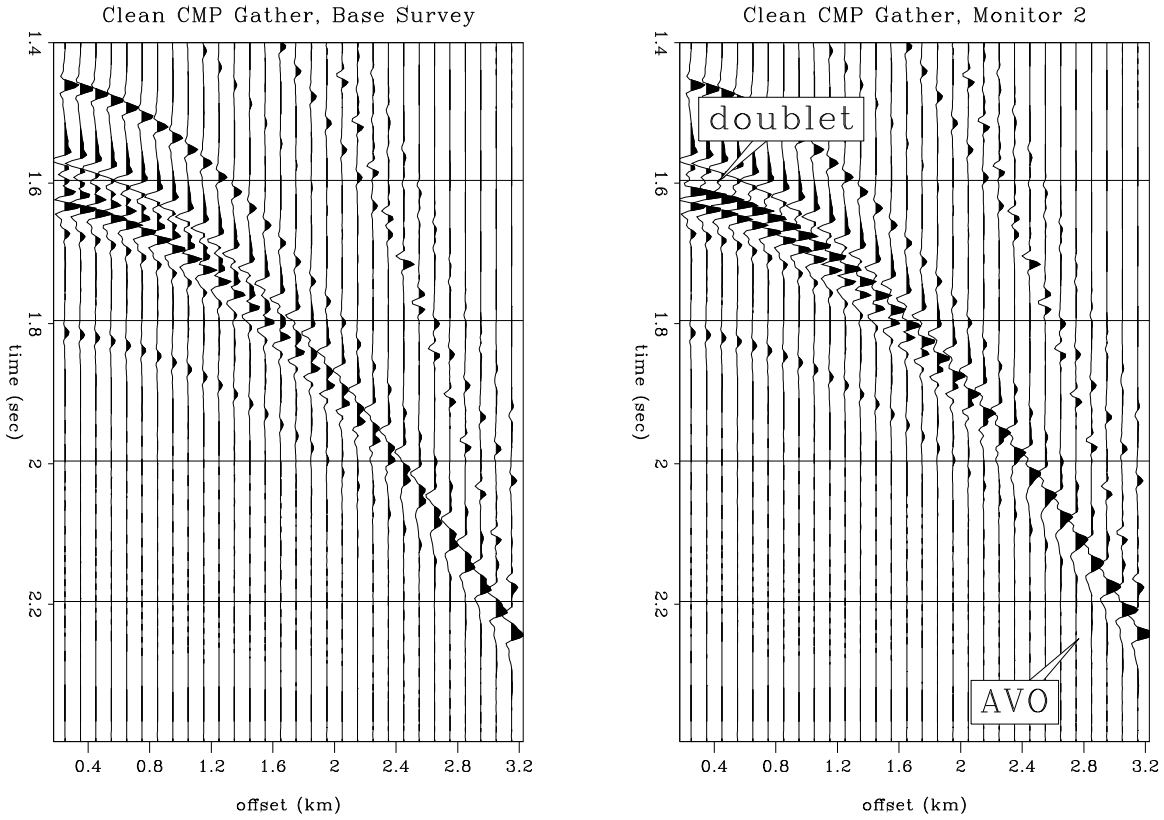

Figure 1.36: Noise-free CMP gathers at the well location, before (left) and after (right) oil depletion. Note the change in waveform at near offsets, and the AVO tuning effect at the far offsets. feas-cmp-clean-ann [CR]

1.5.6 Stacked section analysis

Two prestack marine surveys were simulated to monitor before and after oil depletion in the Troll reservoir. Each survey consisted of 161 60-fold CMP gathers with noise, as described in the previous section. The midpoint spacing was 25 m such that the 161 CMP gathers in each survey covered a total line length of 4 km. Each gather had a minimum source-receiver offset of 250 m and a maximum offset of 3.250 km, and a total record length of 2.4 seconds at a 4 ms sample interval.

The prestack data were muted at water velocity, divergence corrected, and amplitude corrected for source and receiver directivity prior to stacking. No wavelet

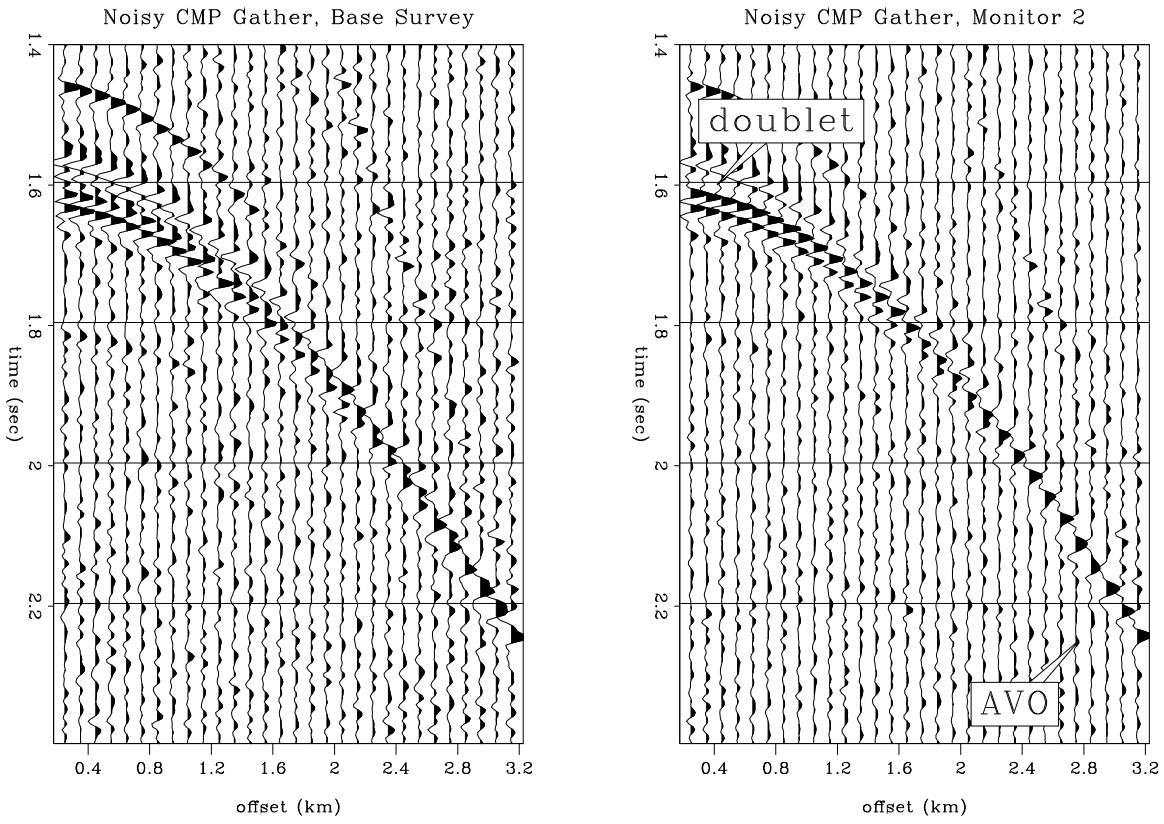

Figure 1.37: Noisy CMP gathers at the well location, before (left) and after (right) oil depletion. The change in waveform at near offset is still visible, but the AVO tuning effect at the far offsets is partially obscured by noise. feas-cmp-noise-ann [CR]

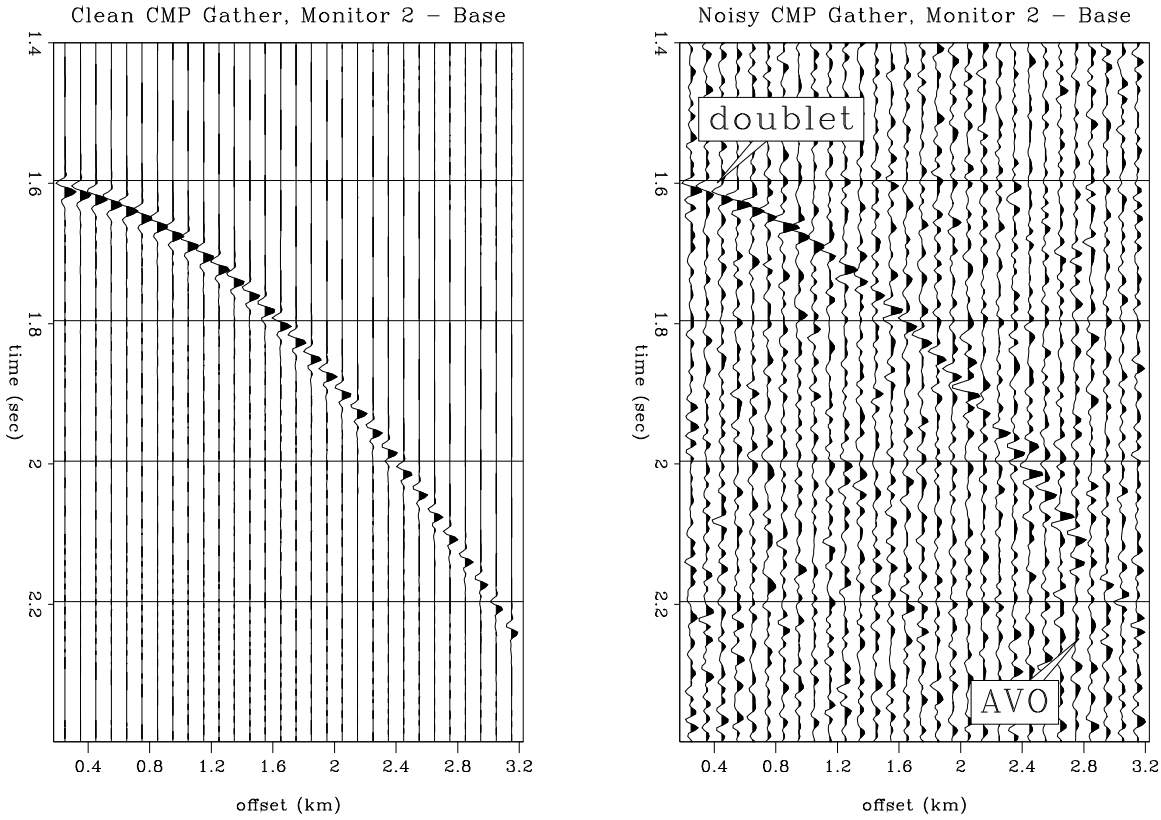

Figure 1.38: Difference CMP gathers at the well location, clean (left) and with added noise (right). Obtained by subtracting the baseline CMP gather from the CMP gather simulated after 113 days of oil depletion. feas-cmp-diff-ann [CR]

deconvolution was applied. A 1-D rms stacking velocity was computed from the 1-D overburden interval velocity model, without the detailed 2-D reservoir zone velocity variations, and was used to perform an anti-aliased NMO stack. This emulates a standard processing sequence in which only macro velocity information is known prior to stacking and migration.

Figure 1.39 shows a close-up of the reservoir in the baseline survey stacked section. Figure 1.40 shows the same reservoir close-up of the monitor stacked section after oil depletion. Subtle changes in the form of increased bright amplitudes in the stacked section are evident in the vicinity of the wellbore and gas coning at 2 km and 1.6 s. Also, some diffraction tails are present due to the point-source-like, strong impedance contrast at the lower tip of the gas cone.

Figure 1.41 shows the difference section obtained by a simple subtraction of the baseline stack from the monitor stack. The gas coning clearly stands out from the background seismic noise as a bright spot at 2 km and 1.6 s. A diffraction tail is present at the tip of the gas cone. Clearly, seismic changes due to oil depletion and gas coning are "detectable" in the seismic monitor sections. However, the resolution of the gas cone is very poor. This is because a stacked section has a lateral resolution that is on the order of a Fresnel zone, typically hundreds of meters wide at this depth, frequency and velocity, as discussed in Chapter 4.

There are some low amplitude seismic differences at the lateral edges of the reservoir, which correspond to small pressure and saturation values from the simulator. These are boundary pressure and saturation changes probably caused by low-amplitude fluid-flow simulation artifacts attributable to a sparse simulation mesh or imperfect boundary conditions in the fluid-flow modeling algorithm.

1.5.7 Prestack migration analysis

The same two prestack datasets described in the previous section were analyzed after prestack migration. Preprocessing included a simple water-velocity mute. No geometrical-spreading correction or source-receiver amplitude directivity were compensated for in the preprocessing phase, since the prestack migration code incorporates these corrections in a more physical manner. An amplitude-preserved Kirchhoff prestack migration code was used that includes operator anti-aliasing (**?**).

Figure 1.42 shows a close-up of the reservoir zone in the baseline survey migrated section. In comparison with the baseline stack of Figure 1.39, one can see the improvement in S/N ratio and increased spatial resolution of the reservoir boundaries and internal reflections that prestack migration brings.

Figure 1.43 shows the prestack migrated reservoir section from the monitor surveys after oil depletion. There is a well-defined increase in bright-spot amplitude at the position of the gas cone, and its spatial resolution is very good compared to the original time-variant impedance models. The migrated sections are not cluttered with diffraction noise as was the case with the stacked sections, and the resolution

of the gas cone anomaly is much higher than the blurred stacked section response. This is because stacked seismic data have a resolution on the range of about one Fresnel zone (typically hundreds of meters), whereas prestack migrated images have a resolution on the order of 1/4 of a seismic wavelength (typically tens of meters), as discussed in Chapter 4.

Figure 1.44 shows the difference section obtained by a simple subtraction of the baseline survey migration from the monitor 1 migration. The gas coning clearly stands out from the background seismic noise as a bright spot at 2 km and 1.6 s, and accurately defines the spatial extent of the true impedance model anomaly.

1.5.8 Survey errors

A question arises as to whether the seismic anomalies observed at these noise levels would still persist given reasonable survey position errors. To examine this effect, I added spatially-correlated random position errors to the source and receiver coordinates of the monitor survey as follows:

- The source depth was given an error with a standard deviation of $\pm$ 2 meters, which is considered to be large. Most airgun arrays can be towed at a constant depth to within at least a 1 meter tolerance.

- The receiver depth was given an error with a standard deviation of $\pm$ 4 meters, which is considered to be extremely large. Hydrophones can be towed within a 1 meter depth tolerance of survey specifications using depth-control "birds" and digital depth meters on the cable.

- All source and receiver positions in the monitor survey were shifted a constant 20 meters in the inline direction compared to the baseline survey. This translational error is considered to be large compared to current differential GPS survey techniques, accurate on the order of a few meters (Paul Segall, pers. comm.).

I simulated new synthetic seismograms for the monitor survey using the altered source and receiver coordinates. I processed the new monitor survey, however, assuming that the altered monitor survey coordinates were identical to the baseline survey coordinates (which is incorrect).

For brevity, I simply present the migration difference section obtained by subtracting the migrated baseline image from the incorrectly processed monitor image (Figure 1.45). Artifacts due to coordinate errors are most visible where the structural dip is the strongest at the fault, and at sharp edges in the model. Most of the artifacts seemed to be caused by the translational error, since the subtraction of geologic structure is most affected. Source and receiver errors, although spatially correlated, are probably averaged out by wavefront healing in the migration process. I conclude that reasonable-to-large survey errors will add some noisy artifacts to the Troll seismic monitor images, but that the main seismic anomaly associated with gas coning will still persist well above typical noise levels.

This analysis indicates that *systematic* position errors may be more harmful to time-lapse seismic monitoring results than *random* position errors. Systematic errors tend to be magnified by geologic structure, and can be misinterpreted as false fluid-flow anomalies in seismic difference sections. Random position errors are probably not harmful if they are much less than 1/4 of a seismic wavelength at the recording surface, and mainly result in a loss of high frequency content in seismic difference sections.

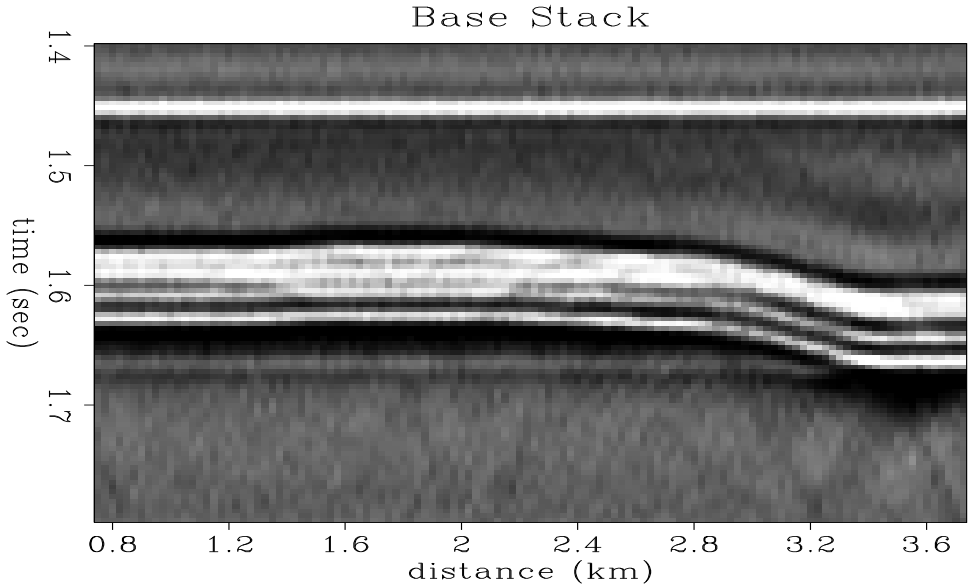

Figure 1.39: Close-up of baseline survey stacked section. feas-stack1 [CR]

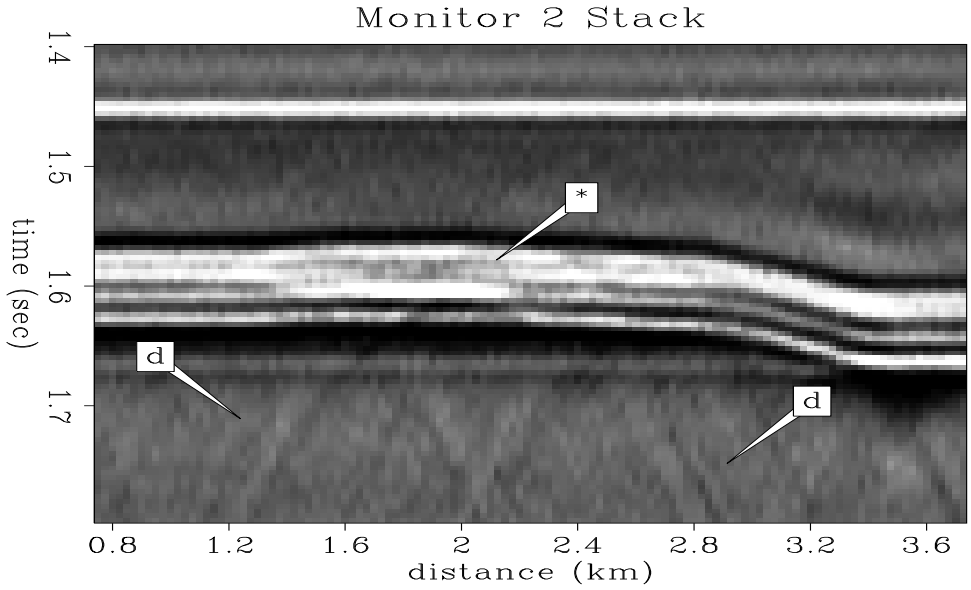

Figure 1.40: Monitor 2 stacked section after 113 days of oil depletion. Note the bright amplitudes due to gas coning, and the development of diffractions "d" from the gas cone. feas-stack3-ann [CR]

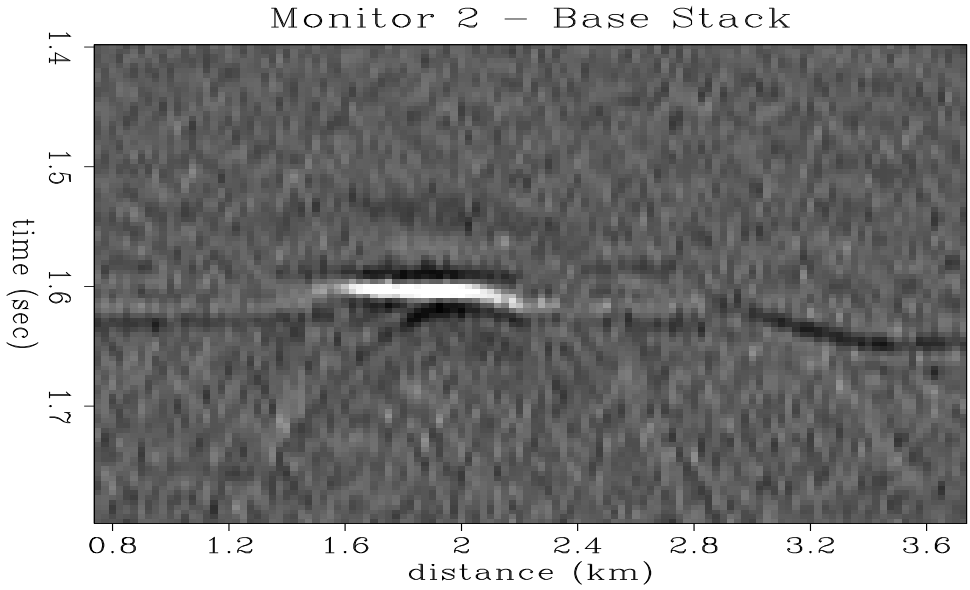

Figure 1.41: Base survey stacked section subtracted from the monitor stacked section. Note the increased bright amplitudes and diffractions due to gas coning. feas-stack13 [CR]

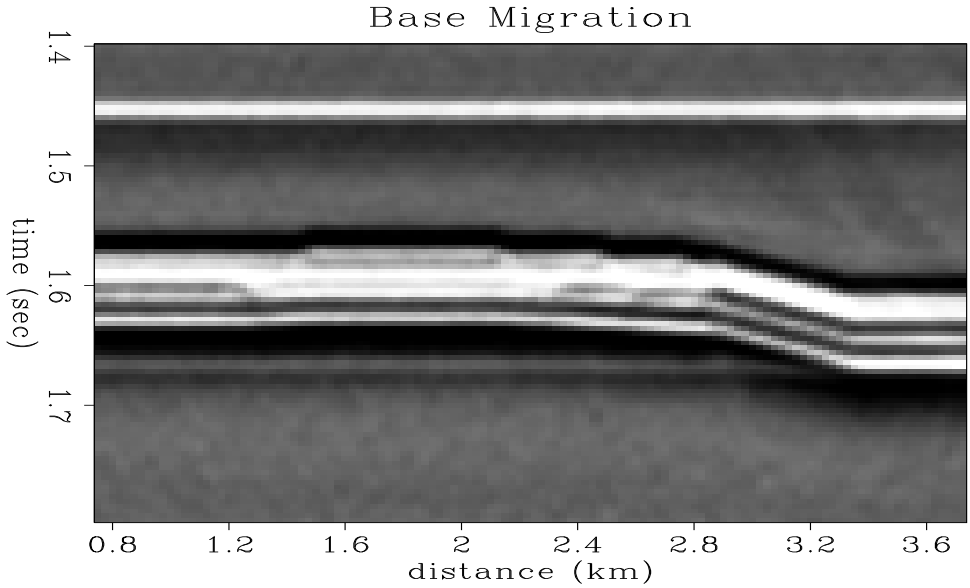

Figure 1.42: Close-up of baseline survey migrated section. feas-mig1 [CR]

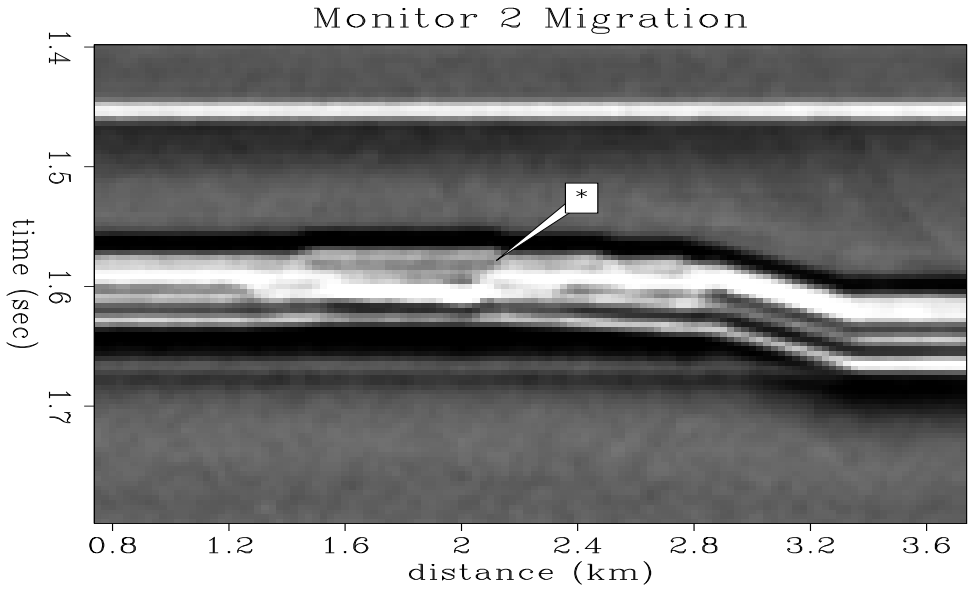

Figure 1.43: Monitor 2 migrated section. Note the bright amplitudes due to gas coning. feas-mig3-ann [CR]

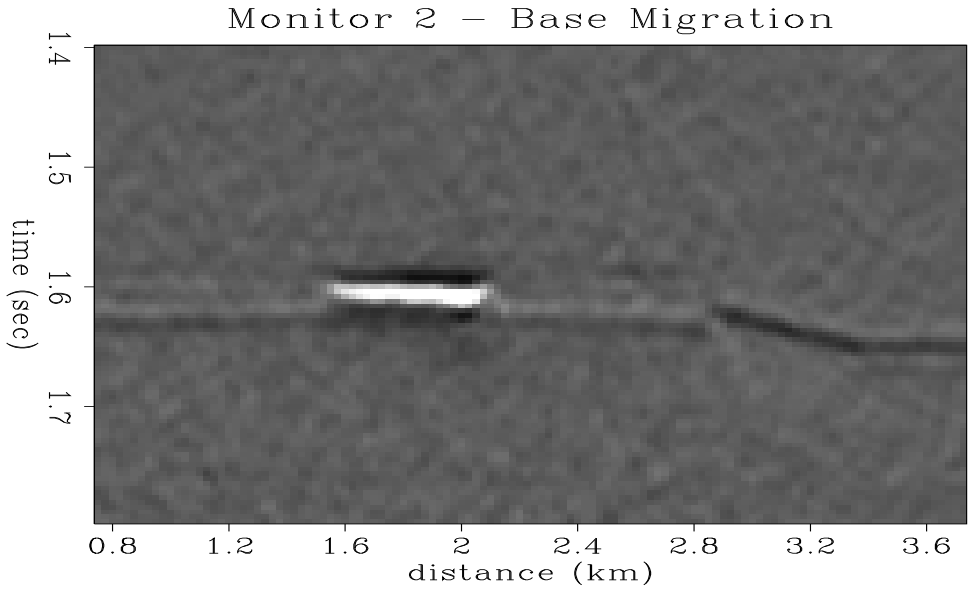

Figure 1.44: Base survey migrated section subtracted from the monitor migrated section. Note the increased bright amplitudes due to gas coning. feas-mig13 [CR]

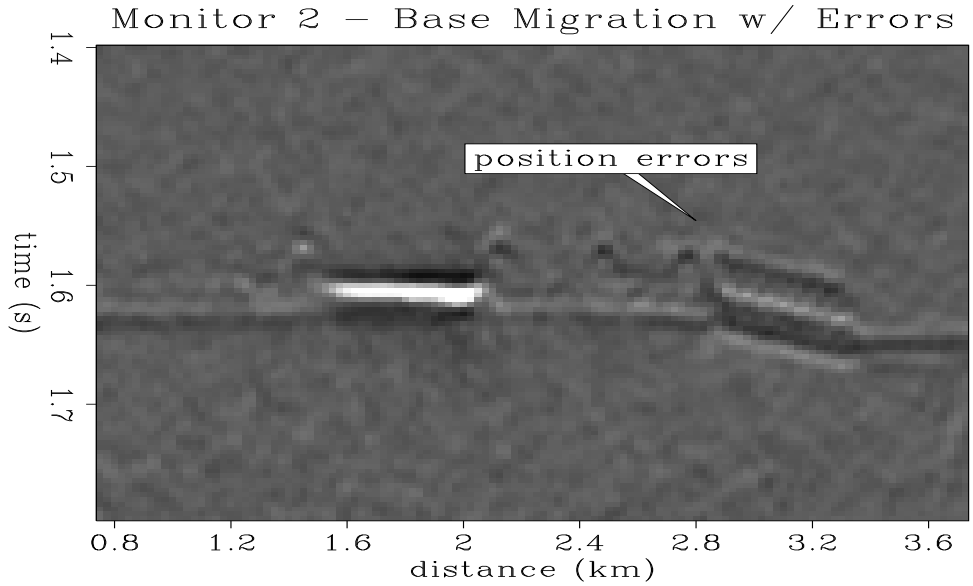

Figure 1.45: Migration difference section with survey errors. Base survey migrated section subtracted from the coordinate-error monitor migrated section. feas-mig14-ann [CR]

1.6 Conclusions

I have conducted a feasibility study to estimate the likelihood of seismically detecting and monitoring the fluid-flow changes in the Troll reservoir during oil depletion from a horizontal well. This hydrocarbon recovery monitoring analysis was conducted by: (1) using flow simulation results (pore pressure, and oil, gas and water saturations) and information about the relevant dry rock properties; (2) using rock physics to compute upscaled compressional and shear wave impedances in the reservoir from the flow simulation results; (3) conducting elastic modeling to simulate seismic surveys of the recovery process; and (4) mapping the difference between seismic responses at a production interval of 113 days, and the baseline seismic survey. Using realistic marine seismic recording geometry parameters and noise levels, I predict that one could successfully detect and monitor gascap expansion and coning in the Troll reservoir from seismic monitor data acquired during oil depletion from a horizontal borehole. Furthermore, the seismic monitoring anomaly would be somewhat degraded, but still coherent above the noise levels in the presence of reasonable survey position errors.

In particular, the prestack migrated sections have enough spatial resolution to accurately locate the lateral extent, depth and thickness of the developing gas cone. If a simple detection of reservoir change is the first order goal, then this could be reasonably achieved after 113 days of oil depletion by comparing the baseline seismic survey stacked section to the monitor survey stacked section using the differencing technique. If, however, a clear image of the dynamic gas-cone evolution is desired, repeated seismic monitoring of oil production is needed to increase the S/N ratio of the

seismic gas-cone response, and robust prestack-migration imaging is required to optimally estimate the spatial extent and amplitude of the evolving gas-cone impedance anomaly. Feasibility studies such as this may help reduce the financial risk associated with designing and implementing a seismic monitoring project given a pre-monitor engineering and petrophysical reservoir database.

1.7 Acknowledgments

The Troll feasibility study was done in collaboration with Amos Nur, Jack Dvorkin and James Packwood of the Stanford Rock and Borehole Consortium. The rock physics component of this research would have been tremendously more difficult without their guidance and efforts. Special thanks goes to Sverre Strandenes of Norsk Hydro for providing the reservoir information, fluid-flow simulation data, financial support, and continued encouragement necessary to undertake this feasibility analysis. I thank Francis Muir, Gary Mavko and Tapan Mukerji for useful discussions and assistance related to this study.